PHYSICAL REVIEW A **90**, 053813 (2014)

Photon-pair generation in nonlinear metal-dielectric one-dimensional photonic structures

D. Javůrek[*] and J. Svozilík
RCPTM, Joint Laboratory of Optics of Palacký University and Institute of Physics of AS CR, 17. listopadu 12,
771 46 Olomouc, Czech Republic

J. Peřina, Jr.
Institute of Physics, Joint Laboratory of Optics of Palacký University and Institute of Physics of AS CR, 17. listopadu 50a,
771 46 Olomouc, Czech Republic

(Received 10 June 2014; published 7 November 2014)

Nonlinear metal-dielectric layered structures are shown to be able to efficiently generate entangled photon pairs using spontaneous parametric down-conversion. Increase of electric-field amplitudes in these structures enhanced by the presence of metal layers is sufficient to compensate for losses inside thin metal layers. As an example, photon pairs emitted from a structure composed of alternating nonlinear dielectric GaN layers and metal Ag layers are analyzed in spectral, temporal, as well as spatial domains. Also, correlations and entanglement between two photons in a pair are determined. Very narrow photon-pair spectra together with strong directionality of photon-pair emission are observed making the photons suitable for photon-atom interactions. Highly enhanced electric-field amplitudes provide high photon-pair generation efficiencies.

DOI: 10.1103/PhysRevA.90.053813 PACS number(s): 42.65.Lm, 42.70.Qs, 68.65.Ac

I. INTRODUCTION

Spontaneous parametric down-conversion (SPDC) is a quantum nonlinear process that was predicted in 1961 [1] and experimentally observed for the first time in 1968 [2,3]. SPDC occurs in nonlinear media with nonzero second-order nonlinear susceptibility tensor $\chi^{(2)}$. During this process, the conservation law of energy originating in homogeneity of time is fulfilled. Also the conservation law of momentum is usually obeyed, at least for the transverse components of wave vectors of the interacting fields. This law originating in homogeneity of space is approximately valid also for longer homogeneous crystals along the propagation direction. The generation of photon pairs has to fulfill both laws and so photon pairs typically occur in states entangled in frequencies, momenta, orbital angular momenta, or polarizations [4–8].

Phase-matching conditions can only be fulfilled under specific conditions that determine the properties of photon pairs. For this reason, new and efficient sources of photon pairs have been developed using, e.g., periodically poled crystals. Periodical poling which introduces periodical modulation of $\chi^{(2)}$ nonlinearity offers enhanced control of phase matching of the nonlinear process, as well as modification of spectral properties of the emitted photon pairs [9–11].

Modern optical structures that confine the fields in one (layered structures) or two (waveguides, optical fibers) dimensions represent qualitative improvement from the point of view of efficiency of photon-pair generation. The confinement of interacting fields enhances their electric-field amplitudes on one side; it qualitatively changes the conditions for an efficient nonlinear interaction on the other side. The requirement for phase matching of wave vectors is then replaced by the need of large spatial overlap of the electric-field amplitudes of all three interacting fields. As spatial profiles of the electric-field amplitudes depend strongly on parameters and geometry of the structures, much broader possibilities for tailoring properties of the emitted photon pairs exist.

A great deal of attention has been devoted to waveguiding structures including planar or rectangular waveguides and photonic fibers. Two-dimensional confinement, together with sufficiently long structures, provides high absolute conversion efficiencies of SPDC, even three or four orders in magnitude larger compared to typical nonlinear bulk crystals. Efficient SPDC in periodically poled waveguides has been investigated in [12–14]. On the other hand, SPDC in photonic fibers [15–17] provides photon pairs in transverse (guided) modes with radial symmetry that are pivotal for optical-fiber communications. From the perspective of applications in communications, ring and vortex nonlinear silica fibers are promising [18,19].

As already mentioned, nonlinear layered structures confine the fields along their propagation direction. Backscattering of the fields creates a one-dimensional photonic-band structure (PBG) with transmission peaks and forbidden bands [20–23]. The electric-field amplitudes are enhanced by this backscattering, which under suitable conditions gives an efficient nonlinear interaction. However, as the confinement of optical fields occurs only in one dimension, the enhancement of optical fields is considerably weaker compared to waveguiding structures, at least for dielectric structures. On the other hand, there exist the usual transverse phase-matching conditions and the impinging fields can be easily coupled into the modes of the structure [23]. Also, properties of a two-photon state can be efficiently and easily controlled by spatial and temporal spectra of the pump beam. Taking into account the precision of well-established fabrication techniques, one-dimensional PBGs represent promising sources of photon pairs.

Nonlinear dielectric layered structures have been already investigated from the point of view of SPDC. Both semiclassical (stochastic) [21] and quantum models [22,23] of SPDC in dielectric layered structures have been elaborated. These structures have been shown to be able to provide entangled photon pairs antisymmetric with respect to the exchange of signal and idler frequencies [24]. Also, random nonlinear

---

[*] javurek@slo.upol.cz

dielectric layered structures have been analyzed as sources of spectrally ultranarrow photon pairs [25,26]. Surface SPDC has been shown to give important contribution to photon-pair generation rates [27–29].

On the contrary, metal-dielectric layered structures have been investigated from the point of view of transmission properties [30,31]. It has been shown that, considering the overall transmission, the total amount of metal inside the structure can be considerably larger provided that it is split into thin layers sandwiched by dielectric layers. This occurs due to strong backscattering on metal-dielectric boundaries with high contrast of refraction indices. This contrast is not only sufficient for the compensation of losses in metal layers; it also enhances the electric-field amplitudes considerably stronger compared to only dielectric structures [32]. It also allows us to consider efficient nonlinear processes in more complex metal-dielectric structures. Narrow spectral interaction regions and strong directionality of photon emissions are distinguished properties of such structures. For this reason, the emitted photon pairs are suitable for photon-atom interactions that require both properties to maximize the strength of interaction [33]. We note that such photon-atom interaction is in the center of attention in recent years in quantum-information processing as entanglement is easily generated in optical fields but excitations are easily stored in atomic systems [34–36]. Recently, the process of second harmonic generation in metal-dielectric layered structures has been investigated both theoretically and experimentally [37,38]. Also the first brief investigation of SPDC in such structures has confirmed high enhancement of photon-pair generation rates due to strong backscattering occurring at metal-dielectric boundaries with high contrast of refraction indices [39]. In the paper, we extend this investigation to provide a comprehensive study of properties of photon pairs emitted in metal-dielectric layered structures.

Optical nonlinear response of metals can arise due to several physical processes including the Fermi smearing [37], strong redistribution of charges [38,40] and affecting the path of electrons by a strong magnetic field. Other mechanisms leading to nonlinearity are discussed in [38,41]. In this paper, we derive nonlinearity of the considered Ag layers from the action of the Lorentz force on electrons [41]. As for the dielectric layers, we consider GaN that is transparent for the pump field at wavelength $\lambda_p = 400$ nm and thus allows the generation of photon pairs with wavelengths around $\lambda = 800$ nm efficiently detected at the single-photon level by Si-based detectors. Moreover, GaN has sufficiently high $\chi^{(2)}$ nonlinearity and the fabrication of thin layered GaN structures is well mastered.

The paper is organized as follows. The model of SPDC in metal-dielectric layered structures is presented in Sec. II. Physical quantities characterizing the emitted photon pairs are described in Sec. III. In Sec. IV, a metal-dielectric resonator composed of two Ag layers and one GaN layer is analyzed. An efficient structure composed of 11 GaN and Ag layers is suggested and analyzed as a typical example in Sec. V. Temporal properties of the emitted photon pairs are investigated in Sec. VI. Noise originating in losses in metal layers is addressed in Sec. VII. Conclusions are drawn in Sec. VIII. Appendix A brings the derivation of $\chi^{(2)}$ tensor for metals. Extension of the theory quantifying the noise is given in Appendix B.

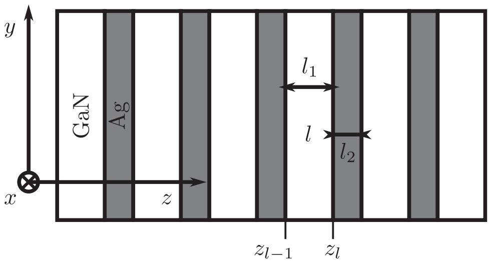

FIG. 1. Scheme of a metal-dielectric layered structure composed of six GaN layers and five Ag layers.

II. MODEL OF SPONTANEOUS PARAMETRIC DOWN-CONVERSION

A vectorial model of SPDC in nonlinear layered structures was formulated in [23] using the interaction Hamiltonian $\hat{H}_{\rm int}$. Alternatively, the interaction momentum operator $\hat{G}_{\rm int}$ can be used to describe SPDC caused by a strong pump beam propagating along the z axis [32,42,43]:

$$\hat{G}_{\rm int}(z) = 2\varepsilon_0 \int_{-\infty}^{\infty} dt \int_{\mathcal{S}} dx dy\ \chi^{(2)}(\mathbf{r}) : \left[\mathbf{E}_p^{(+)}(\mathbf{r},t)\hat{\mathbf{E}}_s^{(-)}(\mathbf{r},t)\hat{\mathbf{E}}_i^{(-)}(\mathbf{r},t) + \text{H.c.}\right]; \quad (1)$$

$\mathbf{r} = (x,y,z)$. The pump field is characterized by its positive-frequency electric-field vector amplitude $\mathbf{E}_p^{(+)}(\mathbf{r},t)$. The signal and idler fields are described by their negative-frequency electric-field operator vector amplitudes $\hat{\mathbf{E}}_s^{(-)}(\mathbf{r},t)$ and $\hat{\mathbf{E}}_s^{(-)}(\mathbf{r},t)$, respectively. Shortening of the tensor of nonlinear susceptibility $\chi^{(2)}$ with respect to its three indices is denoted by :. The symbol ε_0 stands for the vacuum permittivity; H.c. replaces the Hermitian conjugated term. We note that whereas the nonlinear interaction Hamiltonian $\hat{H}_{\rm int}$ gives the interaction energy, the momentum operator $\hat{G}_{\rm int}(z)$ provides the overall flux of this energy through the transverse plane $\mathcal{S}$ positioned at distance z.

The strong undepleted pump field is characterized by its incident temporal spectrum $\mathcal{E}_p(\omega_p)$ and spatial spectrum $\mathcal{E}_p^{\rm tr}(k_{p,x},k_{p,y})$ defined in the transverse plane $\mathcal{S}$. The pump positive-frequency amplitude $\mathbf{E}_p^{(+)}(\mathbf{r},t)$ occurring in Eq. (1) can be decomposed in a layered structure with boundaries localized at positions z_j, $j = 0,\ldots,N$ (for the scheme of the structure, see Fig. 1) as follows:

$$\begin{aligned}\mathbf{E}_p^{(+)}(\mathbf{r},t) = {} & \frac{1}{\sqrt{2\pi}^3 c^2} \int_{-\pi/2}^{\pi/2} |\sin(\vartheta_p)|\, d\vartheta_p \int_{-\pi/2}^{\pi/2} d\psi_p \\ & \times \int_0^{\infty} \omega_p^2 d\omega_p\ \mathcal{E}_p(\omega_p)\mathcal{E}_p^{\rm tr}[k_{p,x}(\mathbf{\Omega}_p),k_{p,y}(\mathbf{\Omega}_p)] \\ & \times \exp[ik_{p,x}(\mathbf{\Omega}_p)x + ik_{p,y}(\mathbf{\Omega}_p)y] \\ & \times \sum_{\gamma=\text{TE,TM}} \sum_{g=F,B} \sum_{l=0}^{N+1} \text{rect}^{(l)}(z) A_{p_g,\gamma}^{(l)}(\mathbf{\Omega}_p)\mathbf{e}_{p,\gamma}^{(l)}(\mathbf{\Omega}_p) \\ & \times \exp\left[ik_{p_g,z}^{(l)}(\mathbf{\Omega}_p)(z - z_{l-1})\right] \exp(-i\omega_p t) \quad (2)\end{aligned}$$

using the notation $\boldsymbol{\Omega}_p \equiv (\omega_p,\vartheta_p,\psi_p)$ for "spherical coordinates" composed of the frequency ω_p, radial propagation angle ϑ_p, and azimuthal propagation angle ψ_p. The scalar electric-field amplitudes $A^{(l)}_{p_F,\gamma}$ and $A^{(l)}_{p_B,\gamma}$ in Eq. (2) characterize the forward- and backward-propagating pump fields, respectively, with γ polarization in an lth layer with index of refraction $n^{(l)}_p$. Polarization vectors $\mathbf{e}^{(l)}_{p_F,\gamma}$ and $\mathbf{e}^{(l)}_{p_B,\gamma}$ determine polarization directions of γ-polarized waves in an lth layer propagating forward (index F) and backward (B), respectively. Function $\text{rect}^{(l)}(z)$ for $l = 1,\ldots,N$ equals 1 for $z_{l-1} \leqslant z < z_l$ and is zero otherwise; function $\text{rect}^{(0)}(z)$ [$\text{rect}^{(N+1)}(z)$] is nonzero only for $z < z_0$ [$z_N \leqslant z$] and equals 1. Speed of light in vacuum is denoted as c. Decomposition of the pump electric-field amplitude $\mathbf{E}^{(+)}_p$ into its TE- and TM-polarized waves [44] in Eq. (2) is done with respect to the plane of incidence of a plane wave with given wave vector $\mathbf{k}_p$.

Cartesian components of the pump-field wave vector $\mathbf{k}_p$ can be written in the form

$$\begin{aligned} k_{p,x}(\boldsymbol{\Omega}_p) &= -\frac{\omega_p \sin(\psi_p)\sin(\vartheta_p)}{c}, \\ k_{p,y}(\boldsymbol{\Omega}_p) &= \frac{\omega_p \cos(\psi_p)\sin(\vartheta_p)}{c}, \\ k^{(l)}_{p_a,z}(\boldsymbol{\Omega}_p) &= \pm\frac{n^{(l)}_p(\omega_p)\omega_p}{c}\cos\left(\vartheta^{(l)}_p\right), \\ l &= 0,\ldots,N+1, \end{aligned} \tag{3}$$

where the radial propagation angle $\vartheta^{(l)}_p$ in an lth layer obeys the Snell law,

$$n^{(0)}_p \sin\left(\vartheta^{(0)}_p\right) = n^{(l)}_p \sin\left(\vartheta^{(l)}_p\right), \quad l = 1,\ldots,N+1, \tag{4}$$

$\vartheta^{(0)}_p \equiv \vartheta_p$. When writing Eq. (3), air around the structure was assumed ($n^{(0)}_p = n^{(N+1)}_p = 1$). As the transverse components of wave vectors do not change during the propagation, the x and y components of wave vector $\mathbf{k}_p$ in Eq. (3) are not indexed. Also, sign + (−) in Eq. (3) corresponds to the forward- (backward-) propagating field.

The signal and idler fields with intensities at single-photon level can be decomposed in the same way as the pump field in Eq. (2). However, instead of coefficients $A^{(l)}_{p_g,\gamma}$ characterizing the classical pump amplitudes, operator coefficients $\hat{A}^{(l)}_{m_a,\alpha}$ describing the quantized signal ($m = s$) and idler ($m = i$) fields are needed [42]. The formula (2) for the pump field can be transformed into the form applicable to the signal and idler fields:

$$\begin{aligned} \hat{\mathbf{E}}^{(+)}_m(\mathbf{r},t) = {} & \frac{1}{\sqrt{2\pi}^3 c^2}\int_{-\pi/2}^{\pi/2} |\sin(\vartheta_m)|\, d\vartheta_m \int_{-\pi/2}^{\pi/2} d\psi_m \\ & \times \int_0^\infty \omega_m^2 d\omega_m \; \exp[ik_{m,x}(\boldsymbol{\Omega}_m)x + ik_{m,y}(\boldsymbol{\Omega}_m)y] \\ & \times \sum_{\gamma=\text{TE,TM}} \sum_{a=F,B} \sum_{l=0}^{N+1} \text{rect}^{(l)}(z)\hat{A}^{(l)}_{m_a,\alpha}(\boldsymbol{\Omega}_m) \\ & \times \mathbf{e}^{(l)}_{m,\alpha}(\boldsymbol{\Omega}_m)\exp\left[ik^{(l)}_{m_a,z}(\boldsymbol{\Omega}_m)(z - z_{l-1})\right] \\ & \times \exp(-i\omega_m t); \quad m = s,i. \end{aligned} \tag{5}$$

Symbols introduced in Eq. (5) have the same meaning for the signal and idler fields as those defined below Eq. (2) for the pump field.

The pump electric-field amplitudes $A^{(l)}_{p_F,\gamma}$ and $A^{(l)}_{p_B,\gamma}$ as well as the signal and idler electric-field operator amplitudes $\hat{A}^{(l)}_{m_F,\alpha}$ and $\hat{A}^{(l)}_{m_B,\alpha}$ occurring in Eqs. (2) and (5), respectively, are mutually coupled through the Fresnel relations at the boundaries and free-space evolution inside the layers. These relations make it possible to express the pump electric-field amplitudes inside the layers in terms of the amplitudes $A^{(0)}_{p_F,\gamma}$ and $A^{(N+1)}_{p_B,\gamma}$ characterizing the forward- and backward-propagating incident pump fields. On the other hand, the same relations applied to the signal and idler fields provide the signal and idler electric-field operator amplitudes inside the layers in terms of operator amplitudes $\hat{A}^{(N+1)}_{m_F,\alpha}$ and $\hat{A}^{(0)}_{m_B,\alpha}$ that correspond to the forward- and backward-propagating outgoing signal and idler fields. The transfer matrix formalism describing these relations has been developed in [23,32,44]. Using quantization of photon flux [45,46], the operator amplitudes $\hat{A}^{(N+1)}_{m_F,\alpha}$ and $\hat{A}^{(0)}_{m_B,\alpha}$ can be written using the annihilation operators $\hat{a}^{(N+1)}_{m_F,\alpha}(\boldsymbol{\Omega}_m)$ and $\hat{a}^{(0)}_{m_B,\alpha}(\boldsymbol{\Omega}_m)$ obeying the usual boson commutation relations:

$$\begin{aligned} \hat{A}^{(N+1)}_{m_F,\alpha}(\boldsymbol{\Omega}_m) &= i\sqrt{\frac{\hbar\omega_m}{2\varepsilon_0 c}}\,\hat{a}^{(N+1)}_{m_F,\alpha}(\boldsymbol{\Omega}_m); \\ \hat{A}^{(0)}_{m_B,\alpha}(\boldsymbol{\Omega}_m) &= i\sqrt{\frac{\hbar\omega_m}{2\varepsilon_0 c}}\,\hat{a}^{(0)}_{m_B,\alpha}(\boldsymbol{\Omega}_m). \end{aligned} \tag{6}$$

The symbol $\hbar$ stands for the reduced Planck constant. More details can be found in [23,32].

An outgoing photon pair in the state $|\psi^{\text{out}}_{s,i}\rangle$ is described by the first-order perturbation solution of the Schrödinger equation written as

$$\left|\psi^{\text{out}}_{s,i}\right\rangle = \frac{i}{\hbar}\int_0^L dz\, \hat{G}_{\text{int}}(z)|\text{vac}\rangle. \tag{7}$$

In Eq. (7), L denotes the structure length and $|\text{vac}\rangle$ means the signal and idler vacuum state.

Substituting Eqs. (1), (2), (5), and (6) into Eq. (7), we reveal the expression for the two-photon state $|\psi^{\text{out}}_{s,i}\rangle$:

$$\begin{aligned} \left|\psi^{\text{out}}_{s,i}\right\rangle = {} & -\frac{2i}{\sqrt{2\pi}^3 c^7}\sum_{l=1}^{N}\sum_{a,b,g=F,B}\sum_{\alpha,\beta,\gamma=\text{TE,TM}} \\ & \times\left[\prod_{m=p,s,i}\int_{-\pi/2}^{\pi/2}|\sin(\vartheta_m)|d\vartheta_m\int_{-\pi/2}^{\pi/2}d\psi_m\int_0^\infty \omega_m^2 d\omega_m\right] \\ & \times\sqrt{\frac{\omega_s\omega_i}{n^{(l)}_s(\omega_s)n^{(l)}_i(\omega_i)}}\;\mathcal{E}_p(\omega_p)\mathcal{E}^{\text{tr}}_p[k_{p,x}(\boldsymbol{\Omega}_p),k_{p,y}(\boldsymbol{\Omega}_p)] \\ & \times\delta(\omega_p - \omega_s - \omega_i)\delta[k_{p,x}(\boldsymbol{\Omega}_p) - k_{s,x}(\boldsymbol{\Omega}_s) - k_{i,x}(\boldsymbol{\Omega}_i)] \\ & \times\delta[k_{p,y}(\boldsymbol{\Omega}_p) - k_{s,y}(\boldsymbol{\Omega}_s) - k_{i,y}(\boldsymbol{\Omega}_i)] \\ & \times\chi^{(2)(l)}(\boldsymbol{\Omega}_p,\boldsymbol{\Omega}_s,\boldsymbol{\Omega}_i) : \mathbf{e}^{(l)}_{p_g,\gamma}(\boldsymbol{\Omega}_p)\mathbf{e}^{(l)*}_{s_a,\alpha}(\boldsymbol{\Omega}_s)\mathbf{e}^{(l)*}_{i_b,\beta}(\boldsymbol{\Omega}_i) \\ & \times L_l f\left[\frac{1}{2}\Delta k^{(l)}_{g,ab,z}(\boldsymbol{\Omega}_p,\boldsymbol{\Omega}_s,\boldsymbol{\Omega}_i)L_l\right]A^{(l)}_{p_g,\gamma}(\boldsymbol{\Omega}_p) \\ & \times\hat{a}^{(l)\dagger}_{s_a,\alpha}(\boldsymbol{\Omega}_s)\hat{a}^{(l)\dagger}_{i_b,\beta}(\boldsymbol{\Omega}_i)|\text{vac}\rangle; \end{aligned} \tag{8}$$

$f(x)=\exp(ix)\sin(x)/x$. Phase mismatch $\Delta k^{(l)}_{g,ab,z}(\mathbf{\Omega}_p,\mathbf{\Omega}_s,\mathbf{\Omega}_i)=k^{(l)}_{p_g,z}(\mathbf{\Omega}_p)-k^{(l)}_{s_a,z}(\mathbf{\Omega}_s)-k^{(l)}_{i_b,z}(\mathbf{\Omega}_i)$ occurs in an lth layer of length $L_l=z_l-z_{l-1}$. We note that there also exist photon pairs emitted at the boundaries [27,28,32] that are not described by Eq. (8). Contribution of this surface SPDC behaves similarly as the analyzed volume contribution given in Eq. (8). It increases the photon-pair generation rates. We want to point out that the second-order susceptibility $\chi^{(2)}$ of metals depends not only on frequencies ω of the interacting fields, but also on their propagation directions described by angles (θ,ψ) (for mode details, see Appendix A). For GaN layers, nonzero elements of the susceptibility tensor $\chi^{(2)}$ take the values [47]

$$\chi^{(2)}_{xxz}=\chi^{(2)}_{xzx}=\chi^{(2)}_{yyz}=\chi^{(2)}_{yzy}=\chi^{(2)}_{zxx}=\chi^{(2)}_{zyy}=10\text{ pm/V},$$
$$\chi^{(2)}_{zzz}=-20\text{ pm/V}.$$

The output state $|\psi^{\text{out}}_{s,i}\rangle$ in Eq. (8) can be further decomposed with respect to the signal and idler propagation directions and field polarizations. Each term describing the signal field at position $\mathbf{r}_s$ and the idler field at position $\mathbf{r}_i$ takes the form

$$\begin{aligned}
&\left|\psi^{\alpha\beta}_{s_a,i_b}(\mathbf{r}_s,\mathbf{r}_i,t)\right\rangle\\
&=\prod_{m=s,i}\left[\frac{1}{c^2}\int_{-\pi/2}^{\pi/2}|\sin\vartheta_m|d\vartheta_m\int_{-\pi/2}^{\pi/2}d\psi_m\int_0^{\infty}\omega_m^2d\omega_m\right]\\
&\quad\times\phi^{\alpha\beta}_{ab}(\mathbf{\Omega}_s,\mathbf{\Omega}_i)\exp[i(\omega_s+\omega_i)t]\\
&\quad\times\exp\left[-i\left(\mathbf{k}^{\text{out}}_{s_a}\mathbf{r}_s+\mathbf{k}^{\text{out}}_{i_b}\mathbf{r}_i\right)\right]\hat{a}^{\dagger}_{s_a,\alpha}(\mathbf{\Omega}_s)\hat{a}^{\dagger}_{i_b,\beta}(\mathbf{\Omega}_i)|\text{vac}\rangle,\\
&a,b=F,B;\quad\alpha,\beta=\text{TE},\text{TM}.
\end{aligned}\qquad(9)$$

Wave vectors $\mathbf{k}^{\text{out}}_{s_a}$ and $\mathbf{k}^{\text{out}}_{i_b}$ are defined outside the structure. Spectral two-photon amplitude $\phi^{\alpha\beta}_{ab}(\mathbf{\Omega}_s,\mathbf{\Omega}_i)$ defined by Eq. (9) gives the probability amplitude of emitting an α-polarized signal photon at frequency ω_s and propagation direction (ϑ_s,ψ_s) together with its β-polarized idler twin at frequency ω_i and propagation direction (ϑ_i,ψ_i) at the outputs a and b of the structure.

III. QUANTITIES CHARACTERIZING PHOTON PAIRS

Spatial and spectral intensity properties of photon pairs [22,32] can be derived from the joint signal-idler photon-number density $n^{\alpha\beta}_{ab}(\mathbf{\Omega}_s,\mathbf{\Omega}_i)$ related to signal [idler] photons with polarization α [β] and frequency ω_s [ω_i] propagating at angles (ϑ_s,ψ_s) [(ϑ_i,ψ_i)] in direction a [b]. Using the formula Eq. (9) for the two-photon state $|\psi^{\alpha\beta}_{s_a,i_b}(\mathbf{r}_s,\mathbf{r}_i,t)\rangle$, the density $n^{\alpha\beta}_{ab}$ can be written as follows:

$$n^{\alpha\beta}_{ab}(\mathbf{\Omega}_s,\mathbf{\Omega}_i)=\frac{|\sin(\vartheta_s)\sin(\vartheta_i)|\omega_s^2\omega_i^2}{c^4}\left|\phi^{\alpha\beta}_{ab}(\mathbf{\Omega}_s,\mathbf{\Omega}_i)\right|^2.\qquad(10)$$

Signal photon-number density $n^{\alpha\beta}_{s,ab}(\mathbf{\Omega}_s)$ is then derived in the form

$$n^{\alpha\beta}_{s,ab}(\mathbf{\Omega}_s)=\int_{-\pi/2}^{\pi/2}d\vartheta_i\int_{-\pi/2}^{\pi/2}d\psi_i\int_0^{\infty}d\omega_i\,n^{\alpha\beta}_{ab}(\mathbf{\Omega}_s,\mathbf{\Omega}_i).\qquad(11)$$

Subsequently, the signal spectral photon-number density $n^{\omega,\alpha\beta}_{s,ab}(\Omega_s)$ is determined along the formula

$$n^{\omega,\alpha\beta}_{s,ab}(\omega_s)=\int_{-\pi/2}^{\pi/2}d\vartheta_s\int_{-\pi/2}^{\pi/2}d\psi_s\,n^{\alpha\beta}_{s,ab}(\mathbf{\Omega}_s).\qquad(12)$$

Similarly, the signal transverse photon-number density $n^{\text{tr},\alpha\beta}_{s,ab}(\vartheta_s,\psi_s)$ characterizing photons propagating in direction (ϑ_s,ψ_s) is determined as

$$n^{\text{tr},\alpha\beta}_{s,ab}(\vartheta_s,\psi_s)=\int_0^{\infty}d\omega_s\,n^{\alpha\beta}_{s,ab}(\mathbf{\Omega}_s).\qquad(13)$$

Intensity correlations between the signal and the idler fields in their transverse planes are described by the joint signal-idler transverse photon-number density $n^{\text{cor},\alpha\beta}_{ab}(\vartheta_s,\psi_s,\vartheta_i,\psi_i)$ characterizing a photon pair with signal [idler] photon propagating along angles (ϑ_s,ψ_s) [(ϑ_i,ψ_i)] in direction a [b]:

$$n^{\text{cor},\alpha\beta}_{ab}(\vartheta_s,\psi_s,\vartheta_i,\psi_i)=\int_0^{\infty}d\omega_s\int_0^{\infty}d\omega_i\,n^{\alpha\beta}_{ab}(\mathbf{\Omega}_s,\mathbf{\Omega}_i).\qquad(14)$$

If a signal photon is detected at angle (ϑ_s^0,ψ_s^0), the joint signal-idler transverse photon-number density $n^{\text{cor},\alpha\beta}_{ab}(\vartheta_s^0,\psi_s^0,\vartheta_i,\psi_i)$ gives the probability of detecting the accompanying idler photon at direction (ϑ_i,ψ_i). This probability determines the shape of the correlated area [48].

In the time domain, two-photon states are characterized by a two-photon temporal amplitude $\mathcal{A}(\tau_s,\tau_i)$ that gives the probability amplitude of detecting a signal photon at time τ_s together with detecting the accompanying idler photon at time τ_i. Using two-photon spectral amplitude $\phi^{\alpha\beta}_{ab}$ in Eq. (9), the two-photon temporal amplitude $\mathcal{A}(\tau_s,\tau_i)$ can be expressed as

$$\begin{aligned}
&\mathcal{A}^{\alpha\beta}_{ab}(\theta_s,\psi_s,\tau_s,\theta_i,\psi_i,\tau_i)\\
&\quad=\frac{\sqrt{|\sin(\vartheta_s)\sin(\vartheta_i)|}\hbar}{4\pi\varepsilon_0c^3}\int_{-\infty}^{\infty}d\omega_s\int_{-\infty}^{\infty}d\omega_i\sqrt{\omega_s^3\omega_i^3}\phi^{\alpha\beta}_{ab}\\
&\qquad\times(\mathbf{\Omega}_s,\mathbf{\Omega}_i)\exp(-i\omega_s\tau_s)\exp(-i\omega_i\tau_i).
\end{aligned}\qquad(15)$$

Temporal properties of photon pairs are usually experimentally investigated employing the Hong-Ou-Mandel interferometer [49]. In this interferometer, two photons are mutually delayed by τ_l and then they interfere on a beam splitter whose output ports are monitored by two detectors measuring in coincidence. A normalized coincidence-count rate R depends on time delay τ_l according to the formula

$$R^{\alpha\beta}_{ab}(\tau_l,\vartheta_s,\psi_s,\vartheta_i,\psi_i)=1-\rho^{\alpha\beta}_{ab}(\tau_l,\vartheta_s,\psi_s,\vartheta_i,\psi_i),\qquad(16)$$

where

$$\rho_{ab}^{\alpha\beta}(\tau_l,\vartheta_s,\psi_s,\vartheta_i,\psi_i) = \frac{|\sin(\vartheta_s)\sin(\vartheta_i)|\hbar^2}{2c^4 R_{0,ab}^{\alpha\beta}} \int_0^\infty d\omega_s \int_0^\infty d\omega_i \omega_s^3\omega_i^3 \mathrm{Re}\{\phi_{ab}^{\alpha\beta *}(\mathbf{\Omega}_s,\mathbf{\Omega}_i)\phi_{ab}^{\alpha\beta}(\omega_i,\vartheta_s,\psi_s,\omega_s,\vartheta_i,\psi_i)\exp[i(\omega_s-\omega_i)\tau_l]\},$$

$$R_{0,ab}^{\alpha\beta}(\vartheta_s,\psi_s,\vartheta_i,\psi_i) = \frac{|\sin(\vartheta_s)\sin(\vartheta_i)|\hbar^2}{2c^4} \int_0^\infty d\omega_s \int_0^\infty d\omega_i\, \omega_s^3\omega_i^3 |\phi_{ab}^{\alpha\beta}(\mathbf{\Omega}_s,\mathbf{\Omega}_i)|^2. \quad (17)$$

Enhancement of the nonlinear interaction inside a layered structure originates from increased electric-field amplitudes due to backscattering on the boundaries. This enhancement can be quantified using a reference structure defined in [23]. This reference structure uses the natural material nonlinearity exploiting the greatest nonlinear coefficient, but it does not contain any boundary that would scatter the propagating light. The reference structure generates a signal photon in direction (ϑ_s,ψ_s) together with an idler photon in direction (ϑ_i,ψ_i) exploiting phase matching in the transverse plane reached with a pump plane wave found in the spatial spectrum $\mathcal{E}_p^{\rm tr}$. The corresponding two-photon state $|\psi_{s,i}^{\rm ref}\rangle$ is expressed as

$$\begin{aligned}\left|\psi_{s,i}^{\rm ref}\right\rangle = &-\frac{2i}{\sqrt{2\pi}^3 c^5}\left[\prod_{m=s,i}\int_{-\pi/2}^{\pi/2}|\sin(\vartheta_m)|\,d\vartheta_m\right.\\ &\times\left.\int_{-\pi/2}^{\pi/2}d\psi_m\int_0^\infty \omega_m^2 d\omega_m\right]\mathcal{E}_p(\omega_s+\omega_i)\\ &\times\mathcal{E}_p^{\rm tr}[k_{s,x}(\mathbf{\Omega}_s)+k_{i,x}(\mathbf{\Omega}_i),k_{s,y}(\mathbf{\Omega}_s)+k_{i,y}(\mathbf{\Omega}_i)]\\ &\times\sum_{l=1}^N\sqrt{\frac{\omega_s\omega_i}{n_s^{(l)}(\omega_s)n_i^{(l)}(\omega_i)}}\max(|\chi^{(2)(l)}|)\,L_l\\ &\times\hat{a}_s^\dagger(\mathbf{\Omega}_s)\hat{a}_i^\dagger(\mathbf{\Omega}_i)|{\rm vac}\rangle. \end{aligned} \quad (18)$$

Creation operator $\hat{a}_s^\dagger(\mathbf{\Omega}_s)$ $[\hat{a}_i^\dagger(\mathbf{\Omega}_i)]$ describes the signal [idler] photon at the output plane of the structure. Function max gives the maximal value of elements of nonlinear tensor $\chi^{(2)(l)}$. Using the signal photon-number density $n_s^{\rm ref}(\mathbf{\Omega}_s)$ of the reference structure given in Eq. (11), the signal relative photon-number density $\eta_{s,ab}^{\alpha\beta}(\mathbf{\Omega}_s)$ at frequency ω_s and in emission direction (ϑ_s,ψ_s) is conveniently defined using the relation

$$\eta_{s,ab}^{\alpha\beta}(\mathbf{\Omega}_s) = \frac{n_{s,ab}^{\alpha\beta}(\mathbf{\Omega}_s)}{\max_{\vartheta_s,\omega_s}\left[n_s^{\rm ref}(\mathbf{\Omega}_s)\right]}. \quad (19)$$

In Eq. (19), the maximum is taken over the whole interval of radial emission angles ϑ_s and frequencies ω_s assuming a fixed azimuthal emission angle ψ_s^0.

In our numerical calculations, we consider a cw pump field with amplitude ξ_p and a Gaussian transverse profile, i.e.,

$$\mathcal{E}_p(\omega_p) = \xi_p\delta\big(\omega_p-\omega_p^0\big), \quad (20)$$

$$\mathcal{E}_p^{\rm tr}(k_x,k_y) = \frac{r_p}{\sqrt{2\pi}}\exp\left[-\frac{r_p^2\big(k_x^2+k_y^2\big)}{4}\right]; \quad (21)$$

ω_p^0 is the central frequency and r_p stands for the radius of transverse profile. It holds that $\int dk_x\int dk_y|\mathcal{E}_p^{\rm tr}(k_x,k_y)|^2 = 1$. Whenever the expression $\delta^2(\omega)$ occurs in the above-defined formulas, it has to be replaced by the expression $2T/(2\pi)\delta(\omega)$ obtained for the fields defined inside interval $(-T,T)$. Physical quantities obtained per unit time interval are reached in the limit $T\to\infty$.

IV. A SIMPLE METAL-DIELECTRIC RESONATOR

Though both the metal and the dielectric layers are nonlinear, the dielectric layers are able to provide much higher photon-pair fluxes. For this reason, the presence of thin metal layers is important for an enhancement of electric-field amplitudes inside the structure. This enhancement then results in much stronger nonlinear interaction and efficient production of photon pairs. Compared to pure dielectric layered structures like those composed of GaN and AlN, analyzed in [23,32], metal-dielectric layered structures allow for much higher enhancement of electric-field amplitudes due to the high refraction-index contrast of the used metal and dielectric materials. For comparison and considering the wavelength 800 nm, this contrast equals 2.51 [2.16] for GaN [AlN] layers and 5.3 [2.51] for Ag [GaN] layers analyzed here. However, strong attenuation and losses of the electric-field amplitudes occur in metal layers. This puts restrictions to the possible thicknesses of metal layers, as well as to the number of metal layers embedded into the structure.

To get deeper insight into the behavior of metal-dielectric layered structures, we first consider the simplest possible structure composed of only one nonlinear GaN layer sandwiched by two thin Ag layers. Thus, the Ag layers form mirrors of a simple resonator that enhances the electric-field amplitudes inside the GaN layer. To achieve efficient nonlinear interaction, we apply the method for designing an efficient layered structure for SPDC suggested in [23]. Lengths l_2 of GaN layers and l_1 of Ag layer vary in the method to reveal the most efficient structure. In the method, only pairs (l_1,l_2) of lengths that provide transmission maxima for the pump field at a chosen wavelength λ_p^0 are analyzed. Concentrating on the highest transmission maximum that also gives the greatest enhancement of the pump field, the appropriate pairs (l_1,l_2) of lengths form a one-dimensional parametric system. This means that for any value of GaN layer length l_2 there exists only one value of Ag layers length l_1.

In the analysis, we consider a plane-wave TE-polarized pump field at central wavelength $\lambda_p^0 = 400$ nm impinging on the structure at normal incidence. Structures with thick Ag layers ($l_1 > 10$ nm) provide frequency-degenerated photon pairs. On the other hand, structures with thin Ag layers emit frequency nondegenerated photon pairs. The greatest value of relative signal photon-number density η defined in Eq. (19) is reached for slightly frequency nondegenerated photon-pair emission for $l_1 = 9.6376$ nm and $l_2 = 95.1195$ nm. We note

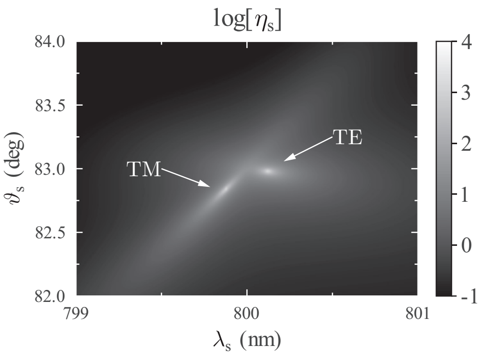

FIG. 2. Topo graph of relative signal photon-number density η_s in dependence on signal radial emission angle ϑ_s and wavelength λ_s for a simple "metal-dielectric" resonator structure composed of one GaN layer and two Ag layers. Both photons with arbitrary polarizations propagate along the $+z$ axis; $\lambda_p^0 = 400$ nm, $l_1 = 95.1195$ nm, $l_2 = 9.6376$ nm, $\psi_s^0 = 0°$; log denotes the decimal logarithm.

that the signal and idler photons can leave the structure along either the $+z$ or the $-z$ axes, so four possible combinations for photon pairs exist. Nevertheless, different photon pairs have comparable properties. That is why we pay attention to only photon pairs with both photons propagating along the $+z$ direction. The structure generates photon pairs around the radial emission angle $\vartheta = 83°$. Two emission maxima in relative signal photon-number density η_s plotted in Fig. 2 are observed. Whereas one maximum contains TE-polarized photons, the other maximum is composed of TM-polarized photons. As elements $\chi^{(2)}_{xxz}$ and $\chi^{(2)}_{xzx}$ of susceptibility tensor participate in the nonlinear interaction, a TE-polarized photon is accompanied by a TM-polarized photon and vice versa. Two maxima in relative signal photon-number density η_s, shown in Fig. 2, are sharp compared to similar dielectric structures. This is a consequence of strong interference of backscattered optical fields caused by the high refractive-index contrast. These sharp features are characteristic for both spectral and spatial properties of photon pairs.

The advantage of "metal resonator" surrounding the nonlinear GaN layer can be quantified comparing its signal photon-number density n_s [Eq. (11)] with that characterizing one GaN monolayer structure of the same length ($l = 114.3947$ nm). Ratio κ of these photon-number densities n_s (see Fig. 3) shows that the enhancement of up to five orders in magnitude is reached in areas of maximal emission intensities, i.e., under conditions of the strongest constructive interference of the signal [idler] field. The enhancement factor rapidly drops down when wavelengths λ_s and radial emission angles ϑ_s move away from these optimal conditions.

V. AN EFFICIENT METAL-DIELECTRIC STRUCTURE

In order to sufficiently enhance the nonlinear interaction, more complex metal-dielectric layered structures have to be considered. There exists an interval of suitable numbers of the used layers. On one side, a larger number of layers leads to strong interference and also to high enhancement of electric-field amplitudes. On the other side, a larger number of metal layers results in strong attenuation of the electric fields. To keep balance between these effects, we have decided to design a structure with five metal Ag layers sandwiched by six GaN layers (for the scheme, see Fig. 1).

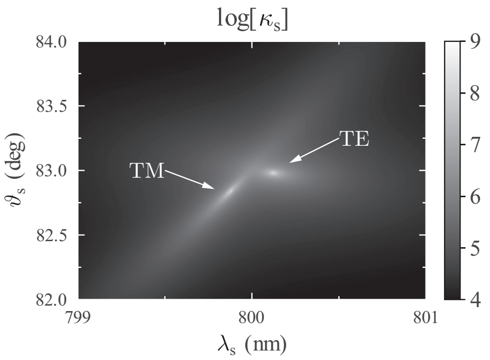

FIG. 3. Topo graph of ratio κ of signal photon-number densities n_s of the simple metal-dielectric resonator structure and GaN monolayer of equal thickness as it depends on signal radial emission angle ϑ_s and wavelength λ_s. Parameters are written in the caption of Fig. 2; log denotes the decimal logarithm.

Following the design procedure, we have plotted the pump-field intensity transmission coefficient T_p at the wavelength $\lambda_p^0 = 400$ nm and for TE polarization [see Fig. 4(a)] as it depends on layers' lengths l_1 and l_2. The pump field impinging on the structure at normal incidence has been assumed. In this

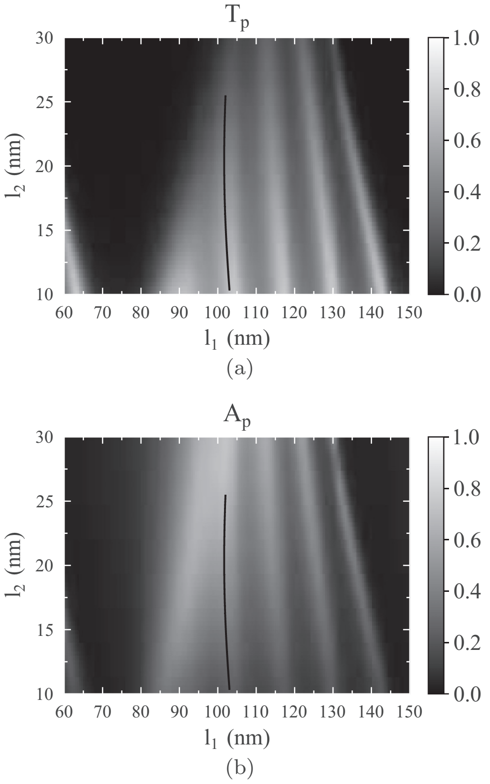

FIG. 4. Topo graphs of (a) the intensity transmission coefficient T_p and (b) the intensity absorption coefficient A_p depending on layers' lengths l_1 and l_2 for TE-polarized field at $\lambda_p^0 = 400$ nm. Positions of maxima in the first transmission band are indicated by solid black curves.

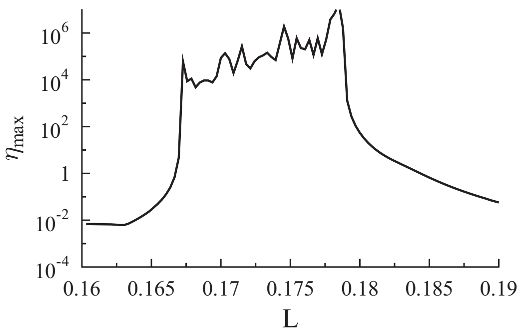

FIG. 5. Maximum $\eta_s^{\max}$ of relative signal photon-number density η_s depending on ratio L of layers' lengths, $L = l_2/l_1$, for structures composed of 11 layers such that the pump field at $\lambda_p^0 = 400$ nm occurs in the center of the first transmission band (see Fig. 4).

graph, five transmission bands can be seen. It follows from the theory of band-gap structures that the greatest enhancement of electric-field amplitudes occurs in the transmission band closest to the band gap. In this band, also the greatest values of absorption A_p are found [see Fig. 4(b)], indicating large electric-field amplitudes inside the metal layers [41].

Structures corresponding to the maxima of the first transmission band have been parameterized by the ratio $L = l_2/l_1$. Maximum $\eta_s^{\max}$ of relative signal photon-number density η_s taken over frequency ω_s and radial emission angle ϑ_s assuming fixed azimuthal angle $\psi_{s,0}$ was chosen for quantification of efficiency of the nonlinear process. Structures with parameter L in the interval (0.1,0.25) were only considered because very thin metal layers do not sufficiently enhance the electric-field amplitudes. Moreover, their transmission bands are broader. On the other hand, thick metal layers attenuate the propagating electric fields. Maximal values $\eta_s^{\max}$ of relative signal photon-number density η_s were found in two regions: $L \in (0.17,0.18)$ and $L \in (0.225,0.24)$. In these regions, $\eta_s^{\max}$ reaches values around 10^6. The first region of L analyzed in Fig. 5 is more suitable and contains the most efficient structure ($L = 0.178$) with lengths $l_1 = 101.752$ nm and $l_2 = 18.083$ nm. The obtained values of maxima $\eta_s^{\max}$ are higher by two orders of magnitude compared to the values of maxima $\eta_s^{\max}$ of the metal resonator investigated in Sec. IV. Additionally, these values are even higher by seven orders of magnitude compared to those of pure dielectric layered structures studied in [23]. Detailed analysis of SPDC inside the metal-dielectric structures shows that dielectric layers are the major source of photon pairs. Metal layers give photon-pair numbers lower by six orders in magnitude compared to the dielectric layers. Nevertheless, they play a critical role in the enhancement of electric-field amplitudes inside the structure due to their high indices of refraction. We have also analyzed SPDC involving a TM-polarized pump field along the same vein. However, the obtained values of maxima $\eta_s^{\max}$ have been found to be considerably lower than those discussed above for the TE-polarized pump field.

Relative signal photon-number density η_s of this structure (plotted in Fig. 6) reveals two emission peaks. One peak is centered at the wavelength $\lambda_s = 737.837$ nm and the radial emission angle $\vartheta_s = 47.686^\circ$ deg, the other peak occurs at the wavelength $\lambda_s = 873.601$ nm and the radial emission angle $\vartheta_s = 61.095^\circ$. The signal photon at wavelength $\lambda_s = 737.837$ nm is TE polarized and its twin has TM polarization. On the other hand, the signal photon at wavelength $\lambda_s = 873.601$ nm has TM polarization, whereas its twin is TE polarized. This means that the first photon pair exploits the element $\chi^{(2)}_{xxz}$ of susceptibility tensor, whereas the second photon pair uses the element $\chi^{(2)}_{xzx}$. The emission peaks are very narrow in both the wavelength λ_s and radial emission angle θ_s. The intensity peaks' widths $\Delta\lambda_s$ are narrower than 1×10^{-3} nm (full width at half maximum, FWHM). In radial emission angle, the intensity peaks' widths $\Delta\theta_s$ are narrower than $5 \times 10^{-2\circ}$. It is worth stressing that the sharpness of these peaks arises from the behavior of TM-polarized fields. The analyzed system has nearly radial symmetry which is only weakly broken by the varying values of $\chi^{(2)}$ elements in azimuthal direction. So the emitted photon pairs form two narrow concentric rings; slightly changing intensities are found around these rings.

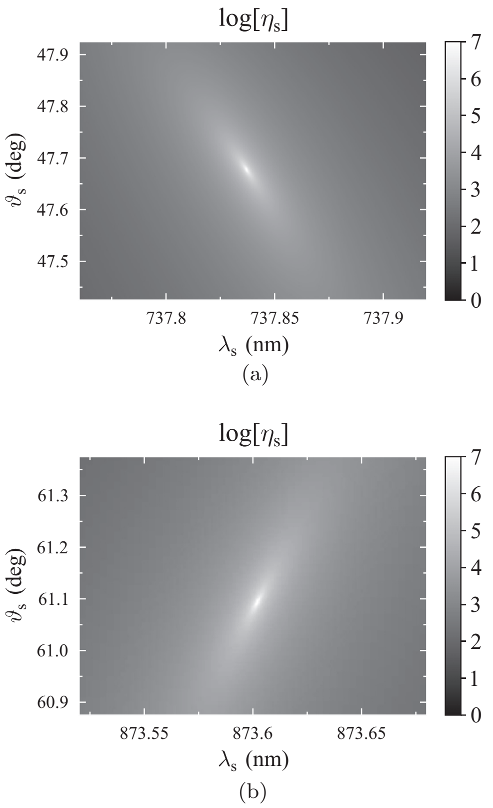

FIG. 6. Topo graphs of relative signal photon-number density η_s in dependence on signal wavelength λ_s and radial emission angle ϑ_s for two regions containing (a) TE-polarized and (b) TM-polarized photons; $\lambda_p^0 = 400$ nm, $l_1 = 101.752$ nm, $l_2 = 18.083$ nm; log denotes the decimal logarithm.

The electric-field amplitude profiles of the interacting fields along the propagating z axis for $(p,s,i) = (\mathrm{TE,TE,TM})$ interaction are shown in Fig. 7. The pump electric-field amplitude profile is determined for the incident electric-field amplitude 1 V/m impinging on the structure at $z = 0$ m. The signal and idler electric-field amplitude profiles are such that they give the outgoing amplitude 1 V/m at the end of the structure and 0 V/m for the outgoing amplitude at $z = 0$ m. The TE-polarized pump and signal fields have their

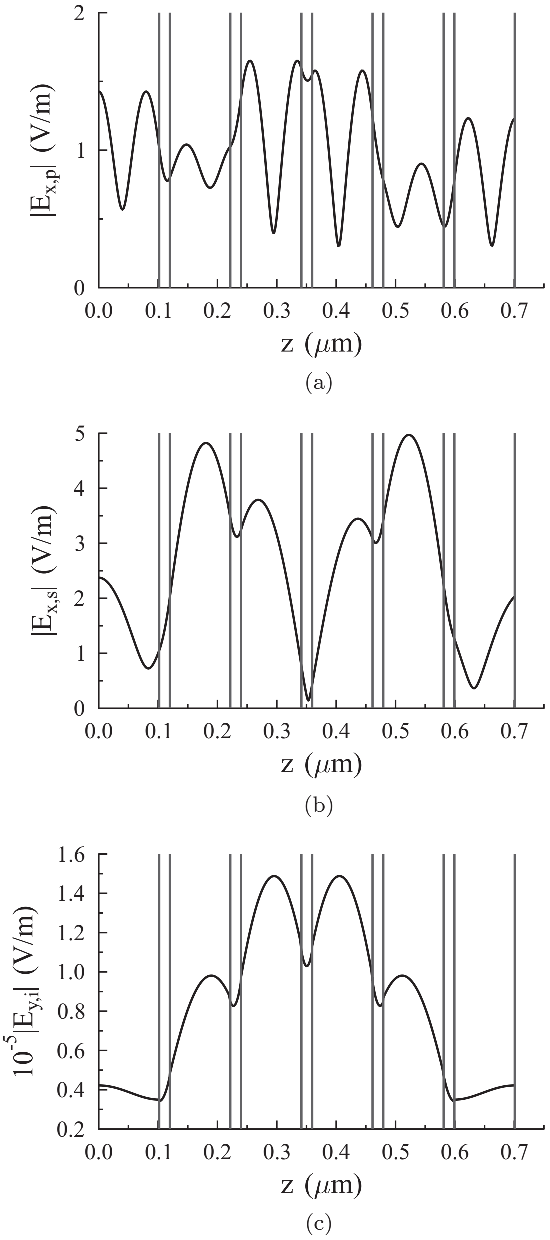

FIG. 7. Profile of the modulus of the electric-field amplitude for (a) pump, (b) signal, and (c) idler fields along the z axis for the pump field with amplitude 1 V/m incident at $z = 0$ m and outgoing signal and idler fields with amplitudes 1 V/m at the end of the structure composed of 11 GaN-Ag layers described in the caption to Fig. 6. In the TM-polarized idler field, the z component of electric-field amplitude is by several orders of magnitude lower than the plotted y component; $\lambda_p = 400$ nm, $\vartheta_p = 0°$, $\lambda_s = 737.8367$ nm, $\vartheta_s = 47.686°$, $\lambda_i = 873.6015$ nm, $\vartheta_i = -61.095°$.

electric-field amplitudes inside the structure enhanced several times. In contrast, the enhancement factor of TM-polarized idler field equals around 10^5 due to highly constructive interference of the backscattered fields at the boundaries. For comparison, the enhancement factor for GaN/AlN layered structures typically equals several tens [23].

Also, correlated areas characterizing spatial correlations between the signal and the idler intensities are narrow. Two different shapes of correlated areas found in the analyzed structure are shown in Fig. 8 for a pump beam with Gaussian transverse profile of radius $r_p = 1$ mm. If we fix the emission direction of the TM-polarized idler photon at $\vartheta_i = -61.095°$, the correlated area of TE-polarized signal photon has roughly a Gaussian shape which originates in the Gaussian pump-field transverse shape [see Fig. 8(a)]. On the other hand, when the TE-polarized signal photon is detected at $\vartheta_s = 47.686°$, the correlated area of TM-polarized idler photon is highly elliptic [see Fig. 8(b)]. The reason is that its extension along the azimuthal angle ψ_i is determined by the pump-beam radius r_p, whereas its extension along the radial angle ϑ_i is strongly limited by the properties of TM modes related to their strong backscattering on the boundaries. The dependence on pump-beam radius r_p can be used to tailor the extensions of correlated areas [48].

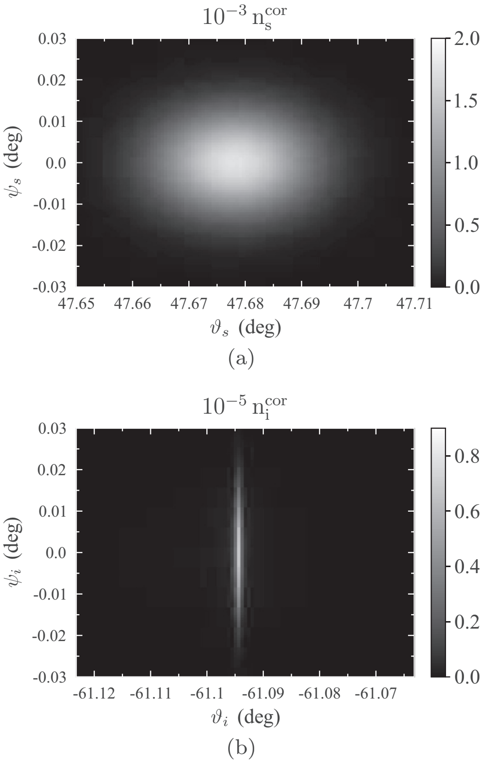

FIG. 8. Correlated area $n^{\rm cor}$ of (a) signal [(b) idler] photon observed after detection of an idler [signal] photon at direction $\vartheta_i^0 = -61.095°$ and $\psi_i^0 = 0°$ [$\vartheta_s^0 = 47.686°$ and $\psi_s^0 = 0°$] for the structure analyzed in Fig. 6. The correlated areas are normalized such that $\int d\vartheta \int d\psi\, n^{\rm cor}(\vartheta,\psi) = (\pi/180)^2$.

VI. TEMPORAL PROPERTIES OF EMITTED PHOTON PAIRS

Due to stationarity, the two-photon spectral amplitude $\phi(\omega_s,\omega_i)$ gets a general form $f_i(\omega_i)\delta(\omega_p^0 - \omega_s - \omega_i)$, in which the δ function expresses the energy conservation law. The squared modulus $|f_i|^2$ is then linearly proportional to the idler spectral photon-number density $n_i^\omega(\omega_i)$. For the analyzed structure, the spectral density n_i^ω of a photon pair with the signal photon propagating along direction $\vartheta_s^0 = 47.686°$ and $\psi_s^0 = 0°$ and the idler photon propagating along direction

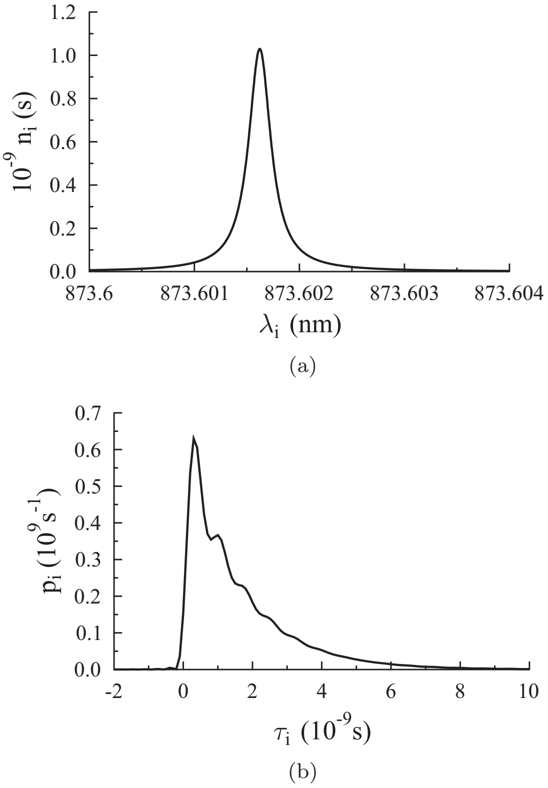

FIG. 9. (a) Idler spectral photon-number density n_i as a function of idler wavelength λ_i and (b) probability density p_i of detecting an idler photon at time τ_i provided that its signal twin was detected at time $\tau_s = 0$ s; $p_i(\tau_i) = C|\mathcal{A}(\tau_s = 0, \tau_i)|^2$ using an appropriate normalization constant C. A photon pair is emitted in directions $\vartheta_s = 47.686^\circ$ and $\psi_s = 0^\circ$ and $\vartheta_i = -61.095^\circ$ and $\psi_i = 0^\circ$ in the structure described in the caption to Fig. 6. Normalization is such that $\int d\omega_i\, n_i(\omega_i) = 1$ and $\int d\tau_i\, p_i(\tau_i) = 1$.

$\vartheta_i^0 = -61.095^\circ$ and $\psi_i^0 = 0^\circ$ attains the form of a very narrow peak of width 4.45×10^{-4} nm [FWHM; see Fig. 9(a)].

The narrow spectral peak is responsible for longer temporal correlations of fields' intensities compared to those characterizing photon pairs generated in typical bulk crystals. For the analyzed structure and cw pumping, intensity temporal correlations occur at the time scale of ns [for the conditional probability density p_i of detecting an idler photon at time τ_i, see Fig. 9(b)]. It is worth noting that the signal- and idler-field group velocities differ considerably. The TE-polarized signal photons propagate, on average, faster than the TM-polarized idler photons that undergo, on average, a much higher number of back reflections on the boundaries after their emission. If pulsed SPDC occurred in the structure, the idler-field detection interval would be much wider than that of the signal field.

Different group velocities of the signal and idler photons inside the structure also result in highly asymmetric coincidence-count rate profiles observed in the Hong-Ou-Mandel interferometer, as documented in Fig. 10. In this interferometer, a much longer average delay of the idler photon has to be compensated by a delay line placed into the signal-photon path to achieve mutual interference of both photons at a beam splitter. Fast oscillations caused by nonzero difference of the signal and idler central frequencies are also visible in the normalized coincidence-count rate R in Fig. 10. We note that the Hong-Ou-Mandel interferometer represents the simplest tool for the observation of temporal correlations between photons.

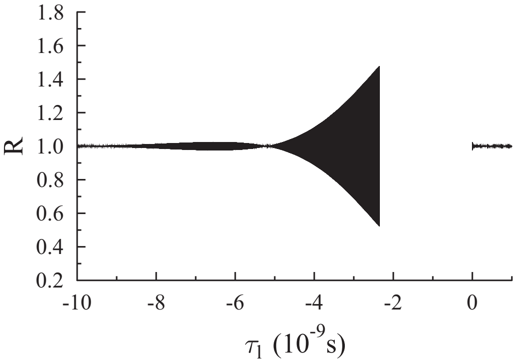

FIG. 10. Normalized coincidence-count rate R in the Hong-Ou-Mandel interferometer depending on mutual time delay τ_l between the signal and the idler photons. The structure described in the caption to Fig. 6 is analyzed.

VII. LOSSES IN THE STRUCTURE AND NOISE PHOTONS

Non-negligible losses occur in the analyzed metal-dielectric layered structures because of the presence of highly absorbing metal layers. When one photon from a photon pair is absorbed whereas the other photon leaves the structure, the emitted joint signal and idler field contains also the single-photon noise present both in the signal and in the idler fields. According to the theory developed in Appendix B, these noise contributions are comparable to the photon-pair one. Ratios $R_{s,FF}^{\rm TE,TM}$ and $R_{i,FF}^{\rm TE,TM}$ given in Eqs. (B5) in Appendix B and quantifying contributions of the signal and idler noise photon-number densities relative to the photon-number densities n_s and n_i given in Eq. (12), respectively, are plotted in Fig. 11. They are appropriate for the structure with 11 layers and the joint signal and idler field composed of the forward-propagating TE-polarized signal and TM-polarized idler photons. Despite the low amount of Ag embedded in the structure (5×18 nm), the numbers of signal and idler noise photons are comparable to the number of emitted photon pairs. Comparable values of ratios $R_{s,FF}^{\rm TE,TM}$ (1.20 for $\vartheta_s = 47^\circ$ and $\lambda_s = 738$ nm) and $R_{i,FF}^{\rm TE,TM}$ (0.97 for $\vartheta_i = 61^\circ$ and $\lambda_i = 834$ nm) for the signal noise and idler noise fields at the corresponding radial emission angles ϑ and for the corresponding frequencies ω indicate that the numbers of emitted noise photons depend mainly on the number of photon pairs generated inside the structure. It is worth noting that the values of ratios $R_{s,FF}^{\rm TE,TM}$ and $R_{i,FF}^{\rm TE,TM}$ increase in the vicinity of forbidden bands, i.e., in the area with strong backscattering and interference (see Fig. 11).

As discussed in Appendix B, photons from photon pairs in which only one photon enters the detection system represent an additional source of the noise. In the analyzed structure, photon pairs with a forward-propagating TE-polarized signal photon and a backward-propagating TM-polarized idler photon contribute to the noise in the signal field. On the other hand, photon pairs with a backward-propagating TE-polarized

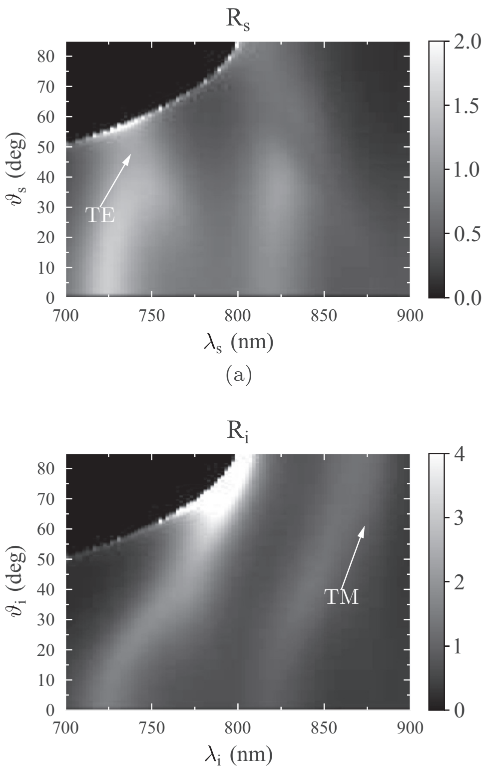

(a)

(b)

FIG. 11. Topo graph of ratio (a) $R_{s,FF}^{\mathrm{TE,TM}}$ [(b) $R_{i,FF}^{\mathrm{TE,TM}}$] of signal [idler] noise photon-number density and photon-pair density in dependence on signal [idler] radial emission angle ϑ_s [ϑ_i] and wavelength λ_s [λ_i] determined along Eq. (B5) in Appendix B. The photon-pair field contains the forward-propagating TE-polarized signal and TM-polarized idler photons; $\lambda_p^0 = 400$ nm, $l_1 = 101.752$ nm, $l_2 = 18.083$ nm.

signal photon and a forward-propagating TM-polarized idler photon are responsible for an additional noise in the idler field. As the numbers of emitted photon pairs with different propagation directions are comparable, the numbers of noise photons constituting these contributions are also comparable. However, these noise contributions can be eliminated if multiple coincidence-count detections are measured.

A considerable amount of the noise present in the generated photon-pair states restricts applicability of such states to the schemes based on coincidence-count measurements. In these schemes, a single-photon noise contributes to the measurement only via random coincidences that are, however, seldom due to the weakness of the field. Possible applications suitable for photon-pair states emitted from metal-dielectric layered structures include quantum cryptography using photon pairs [50] or quantum optical coherence tomography [51], to name few. On the other hand, these states are not suitable for constructing heralded single-photon sources [52].

VIII. CONCLUSIONS

Using quantization of photon flux, a model of SPDC in metal-dielectric layered structures has been developed. Applying this model, an efficient structure composed of six dielectric GaN layers and five metal Ag layers has been designed and analyzed. Highly enhanced electric-field amplitudes caused by metal layers not only compensate for losses in the metal layers; they also allow efficient photon-pair generation in the nonlinear GaN layers. Despite the small number of used layers, the generated photon pairs have very narrow spectra. They are also emitted into very narrow intensity rings in the transverse plane. Compared to a structure consisting of only one GaN monolayer with the same amount of material, the analyzed structure provides photon-pair fluxes greater by seven orders in magnitude. Correlated areas of the emitted photon pairs are very narrow and differ for TE- and TM-polarized fields. Whereas they attain a circular shape for TE-polarized fields and a Gaussian radially symmetric transverse pump-beam profile, they are highly elliptic for TM-polarized fields due to squeezing in the radial direction. Temporal intensity correlations in a photon pair occur at the time scale of ns owing to many backreflections on the boundaries. Compared to nonlinear dielectric layered structures, photon-pair fluxes greater by four orders in magnitude are found. On the other hand, they also generate a single-photon noise originating in broken photon pairs and having photon fluxes comparable to those of photon pairs. Metal-dielectric layered structures provide, in general, the strongly directionally emitted and spectrally narrowband photon pairs necessary, e.g., for quantum-information processing with photons and atoms.

ACKNOWLEDGMENTS

Support by projects CZ.1.05/2.1.00/03.0058 and CZ.1.07/2.3.00/20.0017 of MŠMT ČR and P205/12/0382 of GA ČR are acknowledged. D.J. and J.P. acknowledge support by project IGA_PrF_2014005 of IGA UP Olomouc. J.S. thanks the projects CZ.1.07/2.3.00/30.0004 and CZ.1.07/2.3.00/20.0058 of MŠMT ČR.

APPENDIX A: $\chi^{(2)}$ TENSOR FOR METALS

An expression for tensor $\chi_{jkm}^{(2)}$ of nonlinear susceptibility appropriate for metals containing electrons moving by the Lorentz force caused by an external pump field [41] is derived in this Appendix. Position $\mathbf{r}(t)$ of an electron obeys the equation of motion

$$\frac{d^2\mathbf{r}(t)}{dt^2} + \gamma \frac{d\mathbf{r}(t)}{dt} = -\frac{e}{m}\mathbf{E}(t) - \frac{e}{m}\frac{d\mathbf{r}(t)}{dt} \times \mathbf{B}(t), \qquad \text{(A1)}$$

in which m stands for the electron mass, γ is the collision factor, and e denotes the positive elementary charge. Symbol $\mathbf{E}$ ($\mathbf{B}$) means the electric- (magnetic-) field amplitude. The vector product is denoted as $\times$. Considering mean volume density of electrons N, macroscopic polarization $\mathbf{P}(t)$ is determined by the expression $-eN\mathbf{r}(t)$. Equation (A1) can thus be transformed into an equation for polarization $\mathbf{P}(t)$,

$$\frac{\partial^2\mathbf{P}}{\partial t^2} + \gamma \frac{\partial \mathbf{P}}{\partial t} = \varepsilon_0 \Omega_p^2 \mathbf{E} - \frac{e}{m}\frac{\partial \mathbf{P}}{\partial t} \times \mathbf{B}; \qquad \text{(A2)}$$

$\Omega_p \equiv e\sqrt{N/(\varepsilon_0 m)}$ is the plasma frequency.

The perturbation approach is applied to find the solution of Eq. (A2). Polarization $\mathbf{P}$ is decomposed into strong linear and weak nonlinear parts. Also, the second term on the right-hand side of Eq. (A2) is much smaller than the first one. Solution of Eq. (A2) for three monochromatic waves representing the pump, signal, and idler fields can then be easily found following [53]. It allows us to express the nonlinear tensor $\chi^{(2)}$ as follows:

$$\begin{aligned}\chi^{(2)}_{jlm}(\mathbf{k}_p,\mathbf{k}_s,\mathbf{k}_i) &= -\frac{i\varepsilon_0}{2\pi Ne}\sum_{o,q=x,y,z}\big[L^*(\omega_p)L^*(\omega_s)A(\omega_s,\omega_i)\varepsilon_{jlo}\varepsilon_{oqm}k^*_{i,q}\\ &\quad + L^*(\omega_p)L^*(\omega_i)A(\omega_i,\omega_s)\varepsilon_{imo}\varepsilon_{oql}k^*_{s,q}\\ &\quad + L(\omega_i)L^*(\omega_s)A(\omega_s,\omega_p)\varepsilon_{mlo}\varepsilon_{oqj}k_{p,q}\\ &\quad - L(\omega_i)L(\omega_p)A(\omega_p,\omega_s)\varepsilon_{mjo}\varepsilon_{oql}k^*_{s,q}\\ &\quad - L(\omega_s)L(\omega_p)A(\omega_p,\omega_i)\varepsilon_{ljo}\varepsilon_{oqm}k^*_{i,q}\\ &\quad + L(\omega_s)L^*(\omega_i)A(\omega_i,\omega_p)\varepsilon_{lmo}\varepsilon_{oqj}k_{p,q}\big]. \end{aligned} \tag{A3}$$

In Eq. (A3), ε_{ijk} denotes the Levi-Civita tensor, $L(\omega) = \Omega_p^2/(\omega^2 + i\gamma\omega)$, and $A(\omega,\omega') = \omega/\omega'$. The expression in Eq. (A3) for tensor $\chi^{(2)}$ reveals its strong dependence on frequencies of the interacting fields. Wave vectors $\mathbf{k}$ occurring in Eq. (A3) are assumed to be complex, as the fields are strongly attenuated in metals (due to the skin effect). The expected values of elements of $\chi^{(2)}$ tensor for metals are of the order of 10^{-13} m/V.

APPENDIX B: LOSSES IN LAYERED STRUCTURES AND NOISE PHOTONS

The analyzed metal-dielectric layered structures may produce a considerable amount of noise photons due to strong absorption of the metal. The reason is that an absorbed photon leaves its twin in the structure. If this twin exits the structure, it forms the noise that is superimposed on the emitted photon-pair field. In this Appendix, we develop a theory that quantifies the contribution of noise photons. We assume for simplicity that photon pairs are generated only in dielectric layers, in accord with our results that have revealed only weak generation of photon pairs in metal layers. However, the inclusion of metal layers as sources of photon pairs is straightforward.

A detailed inspection of Eq. (8) for the two-photon state $|\psi^{\rm out}_{s,i}\rangle$ reveals that this state is composed of contributions describing photon pairs emitted in different layers. We assume that similar decomposition can be done also for the joint signal-idler photon-number density $n^{\alpha\beta}_{ab}(\mathbf{\Omega}_s,\mathbf{\Omega}_i)$ defined in Eq. (10):

$$n^{\alpha\beta}_{ab}(\mathbf{\Omega}_s,\mathbf{\Omega}_i) \approx \sum_{l\in\rm diel}\sum_{a',b'=F,B} T^{(l)\alpha}_{s,aa'}(\mathbf{\Omega}_s)T^{(l)\beta}_{i,bb'}(\mathbf{\Omega}_i) \times n^{(l)\alpha\beta}_{a'b'}(\mathbf{\Omega}_s,\mathbf{\Omega}_i). \tag{B1}$$

In Eq. (B1), symbol $n^{(l)\alpha\beta}_{ab}(\mathbf{\Omega}_s,\mathbf{\Omega}_i)$ stands for the joint signal-idler photon-number density of photon pairs emitted in an lth layer. Symbol $\sum_{l\in\rm diel}$ means summation over dielectric layers. The photon-number density $n^{(l)\alpha\beta}_{ab}(\mathbf{\Omega}_s,\mathbf{\Omega}_i)$ is determined along Eq. (10) using a two-photon spectral amplitude $\phi^{(l)\alpha\beta}_{ab}(\mathbf{\Omega}_s,\mathbf{\Omega}_i)$ appropriate for the lth layer. The intensity transmission coefficients $T^{(l)\alpha}_{m,aa'}$ introduced in Eq. (B1) give the probability that an α-polarized photon in field m propagating in direction a' in an lth layer leaves the structure in direction a.

Whereas $T^{(l)\alpha}_{m,Fa'} + T^{(l)\alpha}_{m,Ba'} = 1$ holds for dielectric structures, intensity absorption coefficients $D^{(l)\alpha}_{m,a'}$ are needed in metal-dielectric structures to generalize this relation:

$$T^{(l)\alpha}_{m,Fa'} + T^{(l)\alpha}_{m,Ba'} + D^{(l)\alpha}_{m,a'} = 1; \quad m = s,i; \quad \alpha = \text{TE,TM}; \quad a' = F,B. \tag{B2}$$

The intensity absorption coefficient $D^{(l)\alpha}_{m,a'}$ determines the probability that an α-polarized photon propagating in direction a' in an lth layer in field m is absorbed inside the structure. Using absorption coefficients $D^{(l)\alpha}_{m,a'}$, the signal noise photon-number density $d^{\alpha}_{si,a}(\mathbf{\Omega}_s,\mathbf{\Omega}_i)$ quantifying the amount of single α-polarized photons at frequency ω_s propagating at angle (ϑ_s,ψ_s) in direction a and originating in pairs with an idler photon with frequency ω_i at angle (ϑ_i,ψ_i) is expressed as follows:

$$d^{\alpha}_{si,a}(\mathbf{\Omega}_s,\mathbf{\Omega}_i) = \sum_{l\in\rm diel}\sum_{\beta=\text{TE,TM}}\sum_{a',b'=F,B} T^{(l)\alpha}_{s,aa'}(\mathbf{\Omega}_s) \times D^{(l)\beta}_{i,b'}(\mathbf{\Omega}_i)n^{(l)\alpha\beta}_{a'b'}(\mathbf{\Omega}_s,\mathbf{\Omega}_i). \tag{B3}$$

An overall signal noise photon-number density $d^{\alpha}_{s,a}(\mathbf{\Omega}_s)$ is then simply determined by integrating over all possible idler-field frequencies ω_i and propagation angles (ϑ_i,ψ_i):

$$d^{\alpha}_{s,a}(\mathbf{\Omega}_s) = \int_0^\infty d\omega_i \int_{-\pi/2}^{\pi/2} d\vartheta_i \int_{-\pi/2}^{\pi/2} d\psi_i\, d^{\alpha}_{si,a}(\mathbf{\Omega}_s,\mathbf{\Omega}_i). \tag{B4}$$

Formulas analogous to those written in Eqs. (B3) and (B4) can be derived also for the idler-field noise contribution.

To judge contributions of noise single photons to the generated state with α-polarized signal photons in direction a and β-polarized idler photons in direction b, we define ratios $R^{\alpha\beta}_{m,ab}(\mathbf{\Omega}_m)$ of noise photon-number densities $d^{\alpha}_{s,a}(\mathbf{\Omega}_s)$ and $d^{\beta}_{i,b}(\mathbf{\Omega}_i)$ with respect to densities $n^{\alpha\beta}_{m,ab}(\mathbf{\Omega}_m)$ belonging to photon pairs and written in Eq. (11):

$$R^{\alpha\beta}_{s,ab}(\mathbf{\Omega}_s) = \frac{d^{\alpha}_{s,a}(\mathbf{\Omega}_s)}{n^{\alpha\beta}_{s,ab}(\mathbf{\Omega}_s)}, \quad R^{\alpha\beta}_{i,ab}(\mathbf{\Omega}_i) = \frac{d^{\beta}_{i,b}(\mathbf{\Omega}_i)}{n^{\alpha\beta}_{i,ab}(\mathbf{\Omega}_i)}. \tag{B5}$$

Also, photon pairs with polarizations and propagation directions different from the analyzed one and denoted by indices (a,α) and (b,β) in Eq. (B5) contribute to noise photons provided that one of their two photons is captured by detectors. In this case, ratios $\tilde{R}^{\alpha\beta}_{m,ab}(\mathbf{\Omega}_m)$ defined along the relations

$$\begin{aligned}\tilde{R}^{\alpha\beta}_{s,ab}(\mathbf{\Omega}_s) &= \frac{d^{\alpha}_{s,a}(\mathbf{\Omega}_s) + \sum_{\beta'=\rm TE}^{\rm TM}\sum_{b'=F}^{B} n^{\alpha\beta'}_{s,ab'}(\mathbf{\Omega}_s)}{n^{\alpha\beta}_{s,ab}(\mathbf{\Omega}_s)} - 1,\\ \tilde{R}^{\alpha\beta}_{i,ab}(\mathbf{\Omega}_i) &= \frac{d^{\beta}_{i,b}(\mathbf{\Omega}_i) + \sum_{\alpha'=\rm TE}^{\rm TM}\sum_{a'=F}^{B} n^{\alpha'\beta}_{i,a'b}(\mathbf{\Omega}_i)}{n^{\alpha\beta}_{i,ab}(\mathbf{\Omega}_i)} - 1,\end{aligned} \tag{B6}$$

appropriately characterize the noise of the emitted state. However, this part of noise can be removed, in principle, when multiple coincidence-count measurements are applied in the experiment.

To determine ratios $R^{\alpha\beta}_{m,ab}(\mathbf{\Omega}_m)$ and $\tilde{R}^{\alpha\beta}_{m,ab}(\mathbf{\Omega}_m)$ characterizing noise in the emitted state, we need intensity transmission

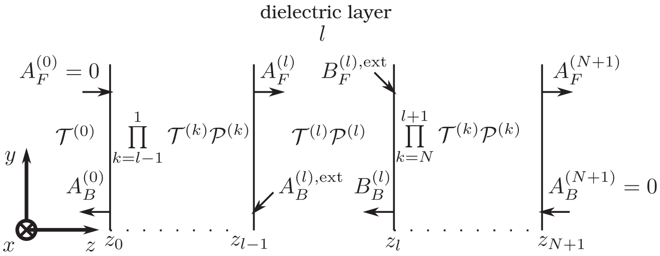

FIG. 12. Scheme of a structure composed of N layers. Whereas amplitudes $A^{(l)}$ describe the fields at the left-hand side of an lth layer ($l = 1,\dots,N+1$), amplitudes $B^{(l)}$ are appropriate for the right-hand side of this layer ($l = 1,\dots,N$); amplitudes $A^{(0)}$ give the fields in front of the structure. Amplitudes $A_B^{(l),\mathrm{ext}}$ and $B_F^{(l),\mathrm{ext}}$ belong to the fields added into an lth layer. Subscript F (B) identifies the forward- (backward-) propagating fields. Matrices $\mathcal{T}^{(l)}$ characterize an lth boundary and matrices $\mathcal{P}^{(l)}$ determine the free-field evolution in an lth layer.

and absorption coefficients for the signal and idler photons born in each dielectric layer. In what follows, we concentrate our attention to field m ($m = s,i$) and an lth layer (for the scheme of a general structure, see Fig. 12). To describe properly damping in metal layers, we have to introduce time into the description, at least implicitly. We reach this by defining the appropriate boundary conditions. We have to distinguish two cases characterizing the photons propagating forward and backward in the lth layer.

We first add to the lth layer backward-propagating α-polarized photons described by amplitude $A_{m_B,\alpha}^{(l),\mathrm{ext}}(\mathbf{\Omega}_m)$ and follow their evolution inside the structure. This evolution is described by the transfer-matrix formalism elaborated for the nonlinear layered structures in [23,32]. The remaining boundary conditions are such that photons do not enter the structure from its front $[A_{m_F,\alpha}^{(0)}(\mathbf{\Omega}_m) = 0]$ and rear $[A_{m_B,\alpha}^{(N+1)}(\mathbf{\Omega}_m) = 0]$ ends. The backward-propagating photons added into the lth layer propagate first in the layers to the left from the lth layer, they can penetrate into the layers to the right from the lth layer later and they can even return back to the left-hand-side layers from the right-hand-side ones. Following the scheme plotted in Fig. 12 and showing the used amplitudes, we can write two sets of linear equations characterizing the propagation through the left- and right-hand-side layers separately:

$$\begin{pmatrix} A_{m_F,\alpha}^{(l)}(\mathbf{\Omega}_m) \\ A_{m_B,\alpha}^{(l),\mathrm{ext}}(\mathbf{\Omega}_m) + \left[\mathcal{P}_m^{(l)}(\mathbf{\Omega}_m)\right]_{22}^{*} B_{m_B,\alpha}^{(l)}(\mathbf{\Omega}_m) \end{pmatrix} = \mathcal{L}_{m,\alpha}^{(l)}(\mathbf{\Omega}_m) \begin{pmatrix} 0 \\ A_{m_B,\alpha}^{(0)}(\mathbf{\Omega}_m) \end{pmatrix},$$

$$\begin{pmatrix} A_{m_F,\alpha}^{(N+1)}(\mathbf{\Omega}_m) \\ 0 \end{pmatrix} = \mathcal{R}_{m,\alpha}^{(l)}(\mathbf{\Omega}_m) \begin{pmatrix} \left[\mathcal{P}_m^{(l)}(\mathbf{\Omega}_m)\right]_{11} A_{m_F,\alpha}^{(l)}(\mathbf{\Omega}_m) \\ B_{m_B,\alpha}^{(l)}(\mathbf{\Omega}_m) \end{pmatrix}. \tag{B7}$$

Matrices $\mathcal{L}_{m,\alpha}^{(l)}(\mathbf{\Omega}_m)$ $[\mathcal{R}_{m,\alpha}^{(l)}(\mathbf{\Omega}_m)]$ introduced in Eq. (B7) describe the propagation of both forward- and backward-propagating fields in the layers positioned to the left [right] from the lth layer. They can be expressed in terms of matrices $\mathcal{T}_{m,\alpha}^{(j)}(\mathbf{\Omega}_m)$ and $\mathcal{P}_m^{(j)}(\mathbf{\Omega}_m)$ characterizing propagation through a jth boundary and free-field propagation in a jth layer, respectively:

$$\mathcal{L}_{m,\alpha}^{(l)}(\mathbf{\Omega}_m) = \prod_{j=l}^{2} \left[\mathcal{T}_{m,\alpha}^{(j-1)}(\mathbf{\Omega}_m)\mathcal{P}_m^{(j-1)}(\mathbf{\Omega}_m)\right]\mathcal{T}_{m,\alpha}^{(0)}(\mathbf{\Omega}_m),$$

$$\mathcal{R}_{m,\alpha}^{(l)}(\mathbf{\Omega}_m) = \prod_{j=N}^{l+1} \left[\mathcal{T}_{m,\alpha}^{(j)}(\mathbf{\Omega}_m)\mathcal{P}_m^{(j)}(\mathbf{\Omega}_m)\right]\mathcal{T}_{m,\alpha}^{(l)}(\mathbf{\Omega}_m). \tag{B8}$$

More details including definitions of the elements of matrices $\mathcal{T}_{m,\alpha}^{(j)}(\mathbf{\Omega}_m)$ and $\mathcal{P}_m^{(j)}(\mathbf{\Omega}_m)$ can be found in [23,32].

Two sets of equations written in (B7) are coupled. These equations can easily be rearranged such that one linear set of equations for amplitudes $A_{m_F,\alpha}^{(N+1)}(\mathbf{\Omega}_m)$, $B_{m_B,\alpha}^{(l)}(\mathbf{\Omega}_m)$, $A_{m_F,\alpha}^{(l)}(\mathbf{\Omega}_m)$, and $A_{m_B,\alpha}^{(0)}(\mathbf{\Omega}_m)$ characterizing the fields leaving the left- and right-hand-side layers is obtained:

$$\begin{pmatrix} 0 \\ 1 \\ 0 \\ 0 \end{pmatrix} A_{m_B,\alpha}^{(l),\mathrm{ext}}(\mathbf{\Omega}_m) = \mathcal{M}_{m,\alpha}^{(l)}(\mathbf{\Omega}_m) \begin{pmatrix} A_{m_F,\alpha}^{(N+1)}(\mathbf{\Omega}_m) \\ B_{m_B,\alpha}^{(l)}(\mathbf{\Omega}_m) \\ A_{m_F,\alpha}^{(l)}(\mathbf{\Omega}_m) \\ A_{m_B,\alpha}^{(0)}(\mathbf{\Omega}_m) \end{pmatrix}, \tag{B9}$$

$$\mathcal{M}_{m,\alpha}^{(l)}(\mathbf{\Omega}_m) = \begin{pmatrix} 0 & 0 & -1 & \left[\mathcal{L}_{m,\alpha}^{(l)}\right]_{12} \\ 0 & -\left[\mathcal{P}_m^{(l)}\right]_{22}^{*} & 0 & \left[\mathcal{L}_{m,\alpha}^{(l)}\right]_{22} \\ -1 & \left[\mathcal{R}_{m,\alpha}^{(l)}\right]_{12} & \left[\mathcal{R}_{m,\alpha}^{(l)}\right]_{11}\left[\mathcal{P}_m^{(l)}\right]_{11} & 0 \\ 0 & -\left[\mathcal{R}_{m,\alpha}^{(l)}\right]_{22} & -\left[\mathcal{R}_{m,\alpha}^{(l)}\right]_{21}\left[\mathcal{P}_m^{(l)}\right]_{11} & 0 \end{pmatrix}. \tag{B10}$$

The solution of Eqs. (B9) provides the output amplitudes that determine photon fluxes both inside the lth layer and outside the whole layered structure. Their analysis provides us the needed intensity transmission and absorption coefficients as follows.

According to the Poynting theorem, time-averaged power $P_{m_B,\alpha}^{(l)}(\mathbf{\Omega}_m)$ generated in the lth layer by the added field $A_{m_B,\alpha}^{(l),\mathrm{ext}}$ is expressed as follows:

$$\begin{aligned} P_{m_B,\alpha}^{(l)}(\mathbf{\Omega}_m) = {} & n_m^{(l)}(\omega_m)\cos\left(\vartheta_m^{(l)}\right) \\ & \times\Big[\left|A_{m_B,\alpha}^{(l),\mathrm{ext}}(\mathbf{\Omega}_m) + \left[\mathcal{P}_m^{(l)}(\mathbf{\Omega}_m)\right]_{22}^{*} B_{m_B,\alpha}^{(l)}(\mathbf{\Omega}_m)\right|^2 \\ & + \left|\left[\mathcal{P}_m^{(l)}(\mathbf{\Omega}_m)\right]_{11} A_{m_F,\alpha}^{(l)}(\mathbf{\Omega}_m)\right|^2 - \left|A_{m_F,\alpha}^{(l)}(\mathbf{\Omega}_m)\right|^2 \\ & - \left|B_{m_B,\alpha}^{(l)}(\mathbf{\Omega}_m)\right|^2\Big]. \end{aligned} \tag{B11}$$

This power is partly dissipated in both the left- and the right-hand-side layers and its remaining part leaves the structure either at its front or rear end. Power $P_{m_B,\alpha}^{(l)F}(\mathbf{\Omega}_m)$ $[P_{m_B,\alpha}^{(l)B}(\mathbf{\Omega}_m)]$ beyond the rear end [in front] of the structure is determined as follows:

$$\begin{aligned} P_{m_B,\alpha}^{(l)F}(\mathbf{\Omega}_m) &= \cos(\vartheta_m)\left|A_{m_F,\alpha}^{(N+1)}(\mathbf{\Omega}_m)\right|^2, \\ P_{m_B,\alpha}^{(l)B}(\mathbf{\Omega}_m) &= \cos(\vartheta_m)\left|A_{m_B,\alpha}^{(0)}(\mathbf{\Omega}_m)\right|^2. \end{aligned} \tag{B12}$$

Power $P_{m_B,\alpha}^{(l)D}(\mathbf{\Omega}_m)$ dissipated in the left- and right-hand-side layers can then be derived from the conservation law of energy:

$$P_{m_B,\alpha}^{(l)D}(\mathbf{\Omega}_m) = P_{m_B,\alpha}^{(l)}(\mathbf{\Omega}_m) - P_{m_B,\alpha}^{(l)F}(\mathbf{\Omega}_m) - P_{m_B,\alpha}^{(l)B}(\mathbf{\Omega}_m). \tag{B13}$$

If power $P^{(l)}_{m_B,\alpha}(\boldsymbol{\Omega}_m)$ equals that of one photon per second, the powers $P^{(l)F}_{m_B,\alpha}(\boldsymbol{\Omega}_m)$, $P^{(l)B}_{m_B,\alpha}(\boldsymbol{\Omega}_m)$, and $P^{(l)D}_{m_B,\alpha}(\boldsymbol{\Omega}_m)$ give, in turn, intensity transmission coefficients $T^{(l)\alpha}_{m,FB}(\boldsymbol{\Omega}_m)$ and $T^{(l)\alpha}_{m,BB}(\boldsymbol{\Omega}_m)$ and intensity absorption coefficient $D^{(l)\alpha}_{m,B}(\boldsymbol{\Omega}_m)$:

$$T^{(l)\alpha}_{m,aB}(\boldsymbol{\Omega}_m) = \frac{P^{(l)a}_{m_B,\alpha}(\boldsymbol{\Omega}_m)}{P^{(l)}_{m_B,\alpha}(\boldsymbol{\Omega}_m)}, \quad a = F,B,$$

$$D^{(l)\alpha}_{m,B}(\boldsymbol{\Omega}_m) = \frac{P^{(l)D}_{m_B,\alpha}(\boldsymbol{\Omega}_m)}{P^{(l)}_{m_B,\alpha}(\boldsymbol{\Omega}_m)}. \qquad \text{(B14)}$$

Now we add to the lth layer forward-propagating α-polarized photons described by amplitude $B^{(l),\mathrm{ext}}_{m_F,\alpha}(\boldsymbol{\Omega}_m)$. These photons propagate first in the right-hand-side layers, they enter into the left-hand-side layers later, and they can propagate back to the right-hand-side layers again. Also in this case, no photon enters the structure from its front $[A^{(0)}_{m_F,\alpha}(\boldsymbol{\Omega}_m) = 0]$ and rear $[A^{(N+1)}_{m_B,\alpha}(\boldsymbol{\Omega}_m) = 0]$ ends. Similarly to that for the added backward-propagating photons, we can write two sets of linear equations characterizing the propagation through the left- and right-hand-side layers separately:

$$\begin{pmatrix} A^{(l)}_{m_F,\alpha}(\boldsymbol{\Omega}_m) \\ \left[\mathcal{P}^{(l)}_m(\boldsymbol{\Omega}_m)\right]^*_{22} B^{(l)}_{m_B,\alpha}(\boldsymbol{\Omega}_m) \end{pmatrix} = \mathcal{L}^{(l)}_{m,\alpha}(\boldsymbol{\Omega}_m) \begin{pmatrix} 0 \\ A^{(0)}_{m_B,\alpha}(\boldsymbol{\Omega}_m) \end{pmatrix},$$

$$\begin{pmatrix} A^{(N+1)}_{m_F,\alpha}(\boldsymbol{\Omega}_m) \\ 0 \end{pmatrix} = \mathcal{R}^{(l)}_{m,\alpha}(\boldsymbol{\Omega}_m) \times \begin{pmatrix} B^{(l),\mathrm{ext}}_{m_F,\alpha}(\boldsymbol{\Omega}_m) + \left[\mathcal{P}^{(l)}_m(\boldsymbol{\Omega}_m)\right]_{11} A^{(l)}_{m_F,\alpha}(\boldsymbol{\Omega}_m) \\ B^{(l)}_{m_B,\alpha}(\boldsymbol{\Omega}_m) \end{pmatrix}. \qquad \text{(B15)}$$

Matrices $\mathcal{L}^{(l)}_{m,\alpha}(\boldsymbol{\Omega}_m)$ and $\mathcal{R}^{(l)}_{m,\alpha}(\boldsymbol{\Omega}_m)$ are defined in Eqs. (B8). Equations (B15) can be transformed into a linear set of equations for amplitudes $A^{(N+1)}_{m_F,\alpha}(\boldsymbol{\Omega}_m)$, $B^{(l)}_{m_B,\alpha}(\boldsymbol{\Omega}_m)$, $A^{(l)}_{m_F,\alpha}(\boldsymbol{\Omega}_m)$, and $A^{(0)}_{m_B,\alpha}(\boldsymbol{\Omega}_m)$ of fields leaving the left- and right-hand-side layers:

$$\begin{pmatrix} 0 \\ 0 \\ -\left[\mathcal{R}^{(l)}_{m,\alpha}(\boldsymbol{\Omega}_m)\right]_{11} \\ \left[\mathcal{R}^{(l)}_{m,\alpha}(\boldsymbol{\Omega}_m)\right]_{21} \end{pmatrix} B^{(l),\mathrm{ext}}_{m,\alpha}(\boldsymbol{\Omega}_m) = \mathcal{M}^{(l)}_{m,\alpha}(\boldsymbol{\Omega}_m) \begin{pmatrix} A^{(N+1)}_{m_F,\alpha}(\boldsymbol{\Omega}_m) \\ B^{(l)}_{m_B,\alpha}(\boldsymbol{\Omega}_m) \\ A^{(l)}_{m_F,\alpha}(\boldsymbol{\Omega}_m) \\ A^{(0)}_{m_B,\alpha}(\boldsymbol{\Omega}_m) \end{pmatrix}; \qquad \text{(B16)}$$

matrix $\mathcal{M}^{(l)}_{m,\alpha}(\boldsymbol{\Omega}_m)$ is defined in Eq. (B10). The solution of Eqs. (B16) allows us to determine photon fluxes that give the powers discussed above. For the forward-propagating photons added into the lth layer, power $P^{(l)}_{m_F,\alpha}(\boldsymbol{\Omega}_m)$ given into this layer by the external field with amplitude $B^{(l),\mathrm{ext}}_{m_F,\alpha}$ is derived in the form

$$\begin{aligned} P^{(l)}_{m_F,\alpha}(\boldsymbol{\Omega}_m) &= n^{(l)}_m(\omega_m)\cos\left(\vartheta^{(l)}_m\right) \\ &\times \Big[\left| B^{(l),\mathrm{ext}}_{m_F,\alpha}(\boldsymbol{\Omega}_m) + \left[\mathcal{P}^{(l)}_m(\boldsymbol{\Omega}_m)\right]_{11} A^{(l)}_{m_F,\alpha}(\boldsymbol{\Omega}_m) \right|^2 \\ &+ \left| \left[\mathcal{P}^{(l)}_m(\boldsymbol{\Omega}_m)\right]^*_{22} B^{(l)}_{m_B,\alpha}(\boldsymbol{\Omega}_m) \right|^2 - \left| B^{(l)}_{m_B,\alpha}(\boldsymbol{\Omega}_m) \right|^2 \\ &- \left| A^{(l)}_{m_F,\alpha}(\boldsymbol{\Omega}_m) \right|^2 \Big]. \end{aligned} \qquad \text{(B17)}$$

This power can be divided into three parts. Its first part $[P^{(l)F}_{m_F,\alpha}(\boldsymbol{\Omega}_m)]$ is delivered beyond the rear end of the structure, whereas its second part $[P^{(l)B}_{m_F,\alpha}(\boldsymbol{\Omega}_m)]$ is transferred into the space in front of the structure. Finally, the third part $[P^{(l)D}_{m_F,\alpha}(\boldsymbol{\Omega}_m)]$ dissipates inside the metal layers. These powers then serve for the determination of intensity transmission coefficients $T^{(l)\alpha}_{m,FF}(\boldsymbol{\Omega}_m)$ and $T^{(l)\alpha}_{m,BF}(\boldsymbol{\Omega}_m)$ and intensity absorption coefficient $D^{(l)\alpha}_{m,F}(\boldsymbol{\Omega}_m)$. Whereas formulas analogous to those written in Eqs. (B11) and (B12) give powers $P^{(l)F}_{m_F,\alpha}(\boldsymbol{\Omega}_m)$, $P^{(l)B}_{m_F,\alpha}(\boldsymbol{\Omega}_m)$, and $P^{(l)D}_{m_F,\alpha}(\boldsymbol{\Omega}_m)$, expressions derived from those in Eqs. (B13) provide coefficients $T^{(l)\alpha}_{m,FF}(\boldsymbol{\Omega}_m)$, $T^{(l)\alpha}_{m,BF}(\boldsymbol{\Omega}_m)$, and $D^{(l)\alpha}_{m,F}(\boldsymbol{\Omega}_m)$.

---

[1] W. H. Louisell, A. Yariv, and A. E. Siegman, Phys. Rev. **124**, 1646 (1961).
[2] S. E. Harris, M. K. Oshman, and R. L. Byer, Phys. Rev. Lett. **18**, 732 (1967).
[3] D. Magde and H. Mahr, Phys. Rev. Lett. **18**, 905 (1967).
[4] T. E. Keller and M. H. Rubin, Phys. Rev. A **56**, 1534 (1997).
[5] J. Svozilík, M. Hendrych, A. S. Helmy, and J. P. Torres, Opt. Express **19**, 3115 (2011).
[6] J. Svozilík, J. Peřina, Jr., and J. P. Torres, Phys. Rev. A **86**, 052318 (2012).
[7] W. P. Grice, R. S. Bennink, Z. Zhao, K. Meyer, W. Whitten, and R. Shaw, in *Quantum Communications and Quantum Imaging VI*, edited by R. E. Meyers, Y. Shih, and K. S. Deacon, SPIE Conference Series, Vol. 7092 (SPIE, Bellingham, WA, 2008), p. 70920Q.
[8] C. K. Law and J. H. Eberly, Phys. Rev. Lett. **92**, 127903 (2004).
[9] S. E. Harris, Phys. Rev. Lett. **98**, 063602 (2007).
[10] G. Brida, M. V. Chekhova, I. P. Degiovanni, M. Genovese, G. K. Kitaeva, A. Meda, and O. A. Shumilkina, Phys. Rev. Lett. **103**, 193602 (2009).
[11] J. Svozilík and J. Peřina, Jr., Phys. Rev. A **80**, 023819 (2009).
[12] A. Eckstein, A. Christ, P. J. Mosley, and C. Silberhorn, Phys. Rev. Lett. **106**, 013603 (2011).
[13] M. Jachura, M. Karpinski, C. Radzewicz, and K. Banaszek, Opt. Express **22**, 8624 (2014).
[14] R. Machulka, J. Svozilík, J. Soubusta, J. Peřina, Jr., and O. Haderka, Phys. Rev. A **87**, 013836 (2013).
[15] A. B. U'Ren, C. Silberhorn, K. Banaszek, and I. A. Walmsley, Phys. Rev. Lett. **93**, 093601 (2004).
[16] X. Sang, C. Yu, M. K. Islam, and N. Lu, J. Adv. Mater. **8**, 1895 (2006).

[17] E. Y. Zhu, Z. Tang, L. Qian, L. G. Helt, M. Liscidini, J. E. Sipe, C. Corbari, A. Canagasabey, M. Ibsen, and P. G. Kazansky, Phys. Rev. Lett. **108**, 213902 (2012).

[18] D. Javůrek, J. Svozilík, and J. Peřina, Jr., Opt. Express **22**, 23743 (2014).

[19] D. Javůrek, J. Svozilík, and J. Peřina, Jr., Phys. Rev. A **90**, 043844 (2014).

[20] M. Scalora, M. J. Bloemer, A. S. Manka, J. P. Dowling, C. M. Bowden, R. Viswanathan, and J. W. Haus, Phys. Rev. A **56**, 3166 (1997).

[21] M. Centini, J. Peřina, Jr., L. Sciscione, C. Sibilia, M. Scalora, M. J. Bloemer, and M. Bertolotti, Phys. Rev. A **72**, 033806 (2005).

[22] J. Peřina, Jr., M. Centini, C. Sibilia, M. Bertolotti, and M. Scalora, Phys. Rev. A **73**, 033823 (2006).

[23] J. Peřina, Jr., Phys. Rev. A **84**, 053840 (2011).

[24] J. Peřina, Jr., M. Centini, C. Sibilia, M. Bertolotti, and M. Scalora, Phys. Rev. A **75**, 013805 (2007).

[25] J. Peřina, Jr., M. Centini, C. Sibilia, and M. Bertolotti, J. Russ. Laser Res. **30**, 508 (2009).

[26] J. Peřina, Jr., M. Centini, C. Sibilia, and M. Bertolotti, Phys. Rev. A **80**, 033844 (2009).

[27] J. Peřina, Jr., A. Lukš, O. Haderka, and M. Scalora, Phys. Rev. Lett. **103**, 063902 (2009).

[28] J. Peřina, Jr., A. Lukš, and O. Haderka, Phys. Rev. A **80**, 043837 (2009).

[29] V. Peřinová, A. Lukš, and J. Peřina Jr., Phys. Scr. **T153**, 014050 (2013).

[30] M. Scalora, M. J. Bloemer, and C. M. Bowden, Opt. Photonics News **10**, 24 (1999).

[31] M. R. Gadsdon, J. Parsons, and J. R. Sambles, J. Opt. Soc. Am. B **26**, 734 (2009).

[32] J. Peřina, Jr., in *Progress in Optics*, edited by E. Wolf (Elsevier, Amsterdam, 2014), Vol. 59, pp. 89–158.

[33] P. Kolchin, S. Du, C. Belthangady, G. Y. Yin, and S. E. Harris, Phys. Rev. Lett. **97**, 113602 (2006).

[34] J. M. Raimond, M. Brune, and S. Haroche, Rev. Mod. Phys. **73**, 565 (2001).

[35] J. Volz, M. Weber, D. Schlenk, W. Rosenfeld, J. Vrana, K. Saucke, C. Kurtsiefer, and H. Weinfurter, Phys. Rev. Lett. **96**, 030404 (2006).

[36] K. S. Choi, H. Deng, J. Laurat, and H. J. Kimble, Nature (London) **452**, 67 (2006).

[37] N. N. Lepeshkin, A. Schweinsberg, R. S. Bennink, and R. W. Boyd, Phys. Rev. Lett. **93**, 123902 (2004).

[38] M. Scalora, M. A. Vincenti, D. de Ceglia, V. Roppo, M. Centini, N. Akozbek, and M. J. Bloemer, Phys. Rev. A **82**, 043828 (2010).

[39] D. Javůrek, J. Svozilík, and J. Peřina, Jr., in *Wave and Quantum Aspects of Contemporary Optics, Proc. SPIE*, edited by J. Peřina, Jr., L. Nožka, M. Hrabovský, D. Senderáková, W. Urbanczyk, and O. Haderka (SPIE, Bellingham, WA, 2012), Vol. 8697, p. 869727.

[40] P. Ginzburg, A. Hayat, N. Berkovitch, and M. Orenstein, Opt. Lett. **35**, 1551 (2010).

[41] M. C. Larciprete, A. Belardini, M. G. Cappeddu, D. de Ceglia, M. Centini, E. Fazio, C. Sibilia, M. J. Bloemer, and M. Scalora, Phys. Rev. A **77**, 013809 (2008).

[42] L. Mandel and E. Wolf, *Optical Coherence and Quantum Optics* (Cambridge University Press, Cambridge, U.K., 1995).

[43] J. Peřina, Jr. and J. Peřina, in *Progress in Optics*, edited by E. Wolf (Elsevier, Amsterdam, 2000), Vol. 41, pp. 361–419.

[44] P. Yeh, *Optical Waves in Layered Media* (Wiley, New York, 1988).

[45] W. Vogel, D. G. Welsch, and S. Walentowicz, *Quantum Optics* (Wiley-VCH, Weinheim, 2001).

[46] B. Huttner, S. Serulnik, and Y. Ben-Aryeh, Phys. Rev. A **42**, 5594 (1990).

[47] J. Miragliotta, D. K. Winckenden, T. J. Kistenmacher, and W. A. Bryden, J. Opt. Soc. Am. B **10**, 1447 (1993).

[48] M. Hamar, J. Peřina, Jr., O. Haderka, and V. Michálek, Phys. Rev. A **81**, 043827 (2010).

[49] C. K. Hong, Z. Y. Ou, and L. Mandel, Phys. Rev. Lett. **59**, 2044 (1987).

[50] N. Gisin, G. Ribordy, W. Tittel, and H. Zbinden, Rev. Mod. Phys. **74**, 145 (2011).

[51] A. F. Abouraddy, K. C. Toussaint, Jr., A. V. Sergienko, B. E. A. Saleh, and M. C. Teich, J. Opt. Soc. Am. B **19**, 656 (2002).

[52] O. Alibart, D. B. Ostrowsky, P. Baldi, and S. Tanzilli, Opt. Lett. **30**, 1539 (2008).

[53] R. W. Boyd, *Nonlinear Optics*, 2nd ed. (Academic Press, New York, 2003).